NTNU – Trondheim
Norwegian University of
Science and Technology

Synthesis and characterisation of the nanostructured magnesium-lanthanum-nickel alloys for Ni-metal hydride battery applications

Thomas Holm

Norwegian University of Science and Technology
Department of Materials Science and Engineering

Abstract

Affordable price, high abundance of magnesium and high densities of hydrogen in the Mg-based hydrides attract interest to these hydrides tailored for hydrogen and energy storage applications. Ternary La-Mg-Ni hydrogen storage alloys with composition $La_{3-x}Mg_xNi_9$ (x = 0.8-1.2) form a new class of the materials for the negative electrodes in Ni-Metal Hydride (Ni-MH) batteries. The electrochemical discharge capacity of such alloys reaches 400 mAh/g which is 25% greater than that of the commercial AB_5-type based electrodes, 315 mAh/g. The $La_{3-x}Mg_xNi_9$ alloys crystallize with trigonal $PuNi_3$ type of crystal structure. Magnesium replaces lanthanum to form the hybrid $LaNi_5$ + Laves phase structures and favorably changes the thermodynamics of the metal-hydrogen interactions allowing improved performance of the advanced metal hydride battery electrodes.

Differences in melting temperatures of lanthanum, nickel and easily evaporating magnesium and a complexity of the phase equilibria in the La-Mg-Ni system cause difficulties in synthesis of the battery electrode alloys with controlled Mg content and a desired phase-structural composition.

In the present work a La_2MgNi_9 alloy was in focus. Its successful synthesis has been achieved from the alloy melts containing 0-30% of overstoichiometric Mg as compared to La_2MgNi_9 by use of Rapid Solidification performed at various quenching rates, with a copper wheel rotation speed of 3.1, 10.5 and 20.9 m/s. They were analyzed by synchrotron X-ray diffraction (SR XRD) including in situ studies in hydrogen gas performed at Swiss-Norwegian Beam Lines at ESRF, Grenoble, and by Scanning Electron Microscopy (SEM) with electron probe microanalysis (EPMA), Pressure-Composition-Temperature isotherms, hydrogen absorption-desorption cycling and measurements of the electrochemical charge-discharge performances were employed to characterize hydrogenation behaviors of the studied alloys. These studies showed that the melt spinning of the alloy containing 30% weight excess of Mg quenched using wheel spin speed of both

400 and 1000 RPM allowed for the synthesis of the most homogeneous sample with the optimal microstructure and phase-structural composition corresponding to the formation of La_2MgNi_9 with the highest yield.

Variations in magnesium content and selection of optimal conditions for the Rapid Solidification process provide complementary possibilities in improving properties of the studied La-Mg-Ni alloys as hydrogen storage and battery electrode materials and provide a possibility to upscale production of the battery alloys.

This work was performed at Institute for Energy Technology and at Department of Materials Science and Engineering, NTNU.

Preface

This work has been carried out at the Department of Materials Science and Technology, Norwegian University of Science and Technology, Institute for Energy Technology, IFE and at European Synchrotron Research Facility in Grenoble, France between August and December 2011. It is part of a cooperation between NTNU and IFE. This work has so far led to a presentation at the SYNKNOYT conference in January 2012, shown in Appendix A and one not yet finished article shown in Appendix B.

Professor Volodymyr Yartys (Norwegian University of Science and Technology and Institute for Energy Technology) has been the main supervisor during the whole period, while Professor Jan Ketil Solberg (Norwegian University of Science and Technology) has been the co-supervisor. Other persons involved in the work are: Dr. Christopher Nwakwuo (NTNU), Dr. Jan Petter Maehlen (IFE) and Dr. Roman Denys (Physico-Mechanical Institute of the National Academy of Science of Ukraine and IFE).

Acknowledgement

I would like to express my gratitude to my supervisor, Prof. Volodymyr Yartys, for making this work possible and for help and support during the whole period. I also would express my gratitude to my co-supervisor Prof. Jan Ketil Solberg for his support during the project.

I want to thank Dr. Christopher Nwakwuo for his aid in the experimental work and discussion and help during the whole period of this project. Furthermore, I would like to thank Dr. Jan Petter Maehlen and Dr. Roman Denys for their always helpful attitude during the theoretical and practical work. My gratitude also goes to my family, especially Prof. Sverre Holm, Andreas Holm and Rune Holm for help during the editing of the report.

Contents

Chapter 1

Motivation

Since 1990, Nickel Metal Hydride (NiMH) batteries have been commercially available and have reached the market for many applications. For transport applications, a high capacity is necessary as this translates into lighter and smaller battery systems and consequently, longer driving ranges between refueling. Therefore, higher capacity should be reached and one has to look beyond the conventional AB_5 and AB_2 alloys currently used in NiMH batteries.

Due to its high storage capacity of hydrogen and low cost, Mg holds a great potential as an energy storage material. Unfortunately, Mg also shows slow kinetics of hydrogenation, high hydride stability and high working temperatures. Therefore, its hydride might be destabilized to yield a high reversible hydrogen storage capacity.

AB_3 and A_2B_7 phases have shown promising results concerning the amount of Mg that can be accommodated into the lattice [1], and some of the hydrogen storage, structural and electrochemical properties of the alloys have recently been studied at IFE [2]. However, the alloys $(La,Mg)Ni_3$ and $(La,Mg)_2Ni_7$ have shown experimental difficulties in the synthesis of single-phase compounds, and a sample of the correct composition usually requires long annealing time at temperatures of 800-1000°C to reach a single-phase structure.

Melt spinning has shown promise in producing single-phase compounds, and this may result in making the annealing step unnecessary. Along with this, melt spinning leads to the nano-structuring of the alloys, which may give a large number of interfaces and grain boundaries. This fine structure can result in faster sorption kinetics and lower temperatures of hydriding/dehydriding.

Chapter 2

Background

2.1 Hydrogen storage in metallic alloys

2.1.1 Storage mechanism

At the negative electrode, a metallic alloy (M) is used. Generally the reaction of the metal hydride formation is as follows:

$$M + \frac{x}{2} H_2 \xrightleftharpoons[discharge]{charge} MH_x \tag{2.1}$$
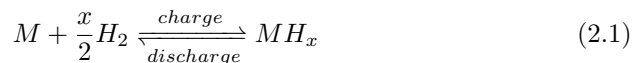
The process of hydrogenation of metals with molecular hydrogen is a metal-gas interaction and can be described as a multistep process. The steps involved in the hydrogenation are:

1. Transport of gaseous hydrogen to the metal surface;

2. Adsorption of hydrogen molecules and the dissociation of H_2 into H-atoms;

3. Hydrogen diffusion into the bulk of the material;

4. Formation of the metal hydride.

Some of these steps may be divided into more steps as well. The total rate of hydride absorption and desorption depends on one or several of these steps. Additives can be used to improve the kinetics of some of the steps, notably

the adsorption and the diffusion step; this is further treated in Section 2.1.5. Another approach to yield better kinetics is to nanostructure the alloy by for example rapid solidification; this will give a material with small grain size and consequently increase the number of interfaces.

The charging of an alloy with hydrogen can also be reached by electrochemical charging. By this mechanism, H^+ is reduced on the surface of the metal yielding atomic H. This is also a multistep mechanism where the total formula is given in Equation 2.7.

2.1.2 Key parameters in hydrogen storage

When classifying the hydrogen storage materials, a number of properties are used. The properties and their meaning are listed below:

1. Total capacity - the total amount of hydrogen that can be stored in the material, given as hydrogen per formula unit [H.f.u.] of hydrogen absorption or desorption at a given temperature;

2. Plateau pressure - the equilibrium pressure at a given temperature. This property is largely coupled with the unit cell volume. A decrease in unit cell volume normally gives an increase in the plateau pressure;

3. Hysteresis - a measure of the difference between the plateau pressures for absorption and desorption, usually given as $ln(\frac{P_{abs}}{P_{des}})$ or $RTln(\frac{P_{abs}}{P_{des}})$;

4. Cyclic stability - the ability of the material to maintain a high reversible hydrogen storage capacity, usually given as a retained capacity after a number of cycles;

5. Ease of activation - a measure of how easy it is to make the hydride from the alloy;

6. High rate properties - how good the material retains it properties if the absorption/desorption steps are done faster;

7. Cost of materials/Ease of manufacture;

Other factors such as safety/inflammability and impurity effects may also be considered.

4
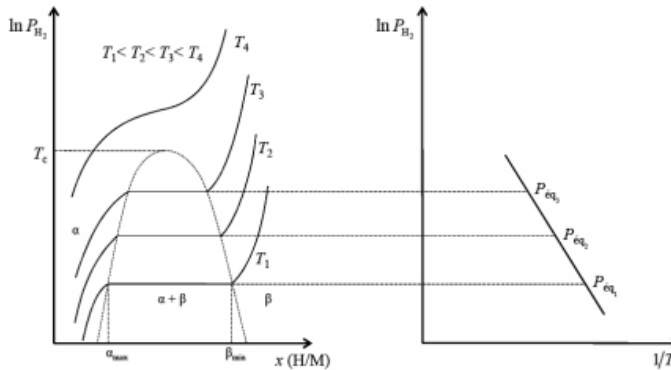
Figure 2.1: *PCT curve with the plotted van't Hoff plot showing how to calculate thermodynamic data by using Equation 2.3 [3].*

2.1.3   Thermodynamics

The thermodynamics of hydride formation/decomposition is determined by measuring at least three PCT plots for the alloy. This gives three different plateau pressures. If the logarithm of these are plotted vs the inverse temperature, this should yield a curve after Equation 2.3. This equation is based on the reaction described in Equation 2.1, which yields the equation for the equilibrium given in Equation 2.2. If the reaction is in equilibrium and hence ΔG is equal to 0, the equation will give the result in Equation 2.3.

$$\Delta G = \Delta H - T\Delta S = -RT \log P_{H_2} \qquad (2.2)$$

$$\log P_{H_2} = -\frac{2}{x}\left(\frac{\Delta H}{RT}\right) + \frac{\Delta S}{R} \qquad (2.3)$$

An example of a PCT plot with the different plateau pressures are plotted in Figure 2.1. Here they are shown alongside the van't Hoff plot so that the enthalpy and entropy can be found.

The standard enthalpy of hydride formation, ΔH, can be found from the slope of the van't Hoff plot. The value for forming a stable hydride with lower equilibrium pressure than 1 bar is $-40\frac{kJ}{mole\,H_2}$ [4]. The entropy of hydride formation, ΔS, is approximately equal for all metal hydrogen systems. This is because the entropy change is dominated by the formation of hydrogen atoms from a gaseous

5

hydrogen molecule [4]. The entropies for the real systems slightly differ from the dissociation entropy of hydrogen gas, $-130 \frac{J}{KmoleH_2}$.

2.1.4 Hydride storage in binary and ternary alloys

Metal hydride storage materials are often denoted with an AB_x formula. The elements taking A and B positions are shown in Figure 2.2. These are grouped due to large differences in electronegativity affecting the bonding between the elements and are rarely overlapping. Some exceptions exists, such as the AB_2-type $TiCr_{1.8}$, where Ti also is in B position, and the formula could have been written $TiCr_{0.89}Ti_{0.11}$.

Figure 2.2: *The periodic table of elements showing which elements are for A position and which are for B position in metal hydrides [3]. (A = red, B = blue).*

2.1.5 Effect of additives

Additives are used to enhance the properties in the alloy. The additives are grouped after which element in the original alloy they are designed to replace. As the original alloy is given as an AB_x, the additives will either replace the A or the B element. Which element is replaced can be determined from Figure 2.2. A-type substitutional element is mostly used to vary the unit cell volume

as this is a property coupled with the plateau pressure. The most common A-type substitutional elements are rare earth metals and especially the naturally occurring mixture called Mischmetal (Mm). This mixture of rare earth elements consists mostly of La, Ce, Pr, Nd and Sm, where La or Ce have the largest fraction. The effect of these elements is largely based on the effect the elements have on the unit cell volume. A decrease in the unit cell volume will give an increase in the plateau pressure. In $LaNi_5$, the largest effect is known for Ce and Sm [5, 6, 7]; these findings have largely been confirmed for AB_3 and A_2B_7 alloys as well [8, 9].The substitution has indicated in some works to improve the cyclic stability and the kinetics of the reaction [9].

B-type additives are relevant for improving the properties of the alloy. The most relevant properties to improve are:

1. Enhancing the corrosion stability;

2. Decreasing the plateau pressure;

3. Increasing the hydrogen storage capacity;

4. Improvement of the kinetics of charge and discharge processes.

The elements used include B, Al, Ti, V, Mn, Co, Fe and Zn. The effect of each element will not be considered in detail here as they are outside the scope of this project.

2.2 Nickel Metal-hydride (NiMH) batteries

In the early 1990's, the first commercial NiMH-batteries were introduced. These batteries were a large improvement as compared to the then common Nickel-Cadmium batteries (NiCd) as they had higher energy density, longer cycle life, better tolerance for overcharge/overdischarge and better environmental compatibility [10]. The chemistry of the NiMH-batteries constitutes of the following electrode reactions:

$$Negative: OH^- + MH \underset{charge}{\overset{discharge}{\rightleftharpoons}} H_2O + M + e^- \qquad (2.4)$$

$$Positive: NiOOH + H_2O + e^- \underset{charge}{\overset{discharge}{\rightleftharpoons}} Ni(OH)_2 + OH^- \qquad (2.5)$$

$$Total: NiOOH + MH \underset{charge}{\overset{discharge}{\rightleftharpoons}} Ni(OH)_2 + M \qquad (2.6)$$
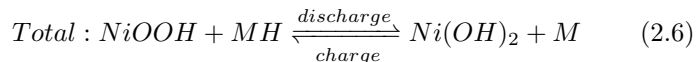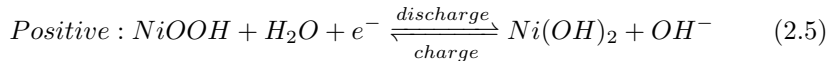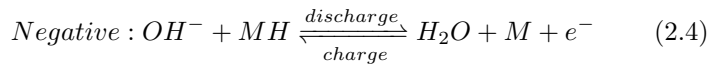
$$E^0 = 1.3V \qquad (2.7)$$

The electrolyte used is normally a 6-8M KOH solution. Upon discharging, hydrogen atoms in the metal hydride dissociate and react with the OH^- to form H_2O, while H_2O at the positive electrode react with the NiOOH to form $Ni(OH)_2$ and OH^-. Upon charging, the reverse reactions occur. Thus, the reactions occurring are in total a movements of hydrogen from one electrode to the other, hence the expression, "rocking-chair" mechanism. The total reaction has 1.3V as the maximum voltage possible, and this value is independent of pH. The real obtained voltage is somewhat lower due to overpotential from sources such as build up of double layer, electrolyte resistance, side reactions and activation. Side reactions occurring in the cell are most notably the two given in Equation 2.8-2.9. These are here given for the charge reaction for the different electrodes.

$$Negative: H_2O + \frac{1}{2}O_2 + 2e^- \rightarrow 2OH^- \qquad (2.8)$$

$$Positive: 2OH^- \rightarrow H_2O + \frac{1}{2}O_2 + 2e^- \qquad (2.9)$$
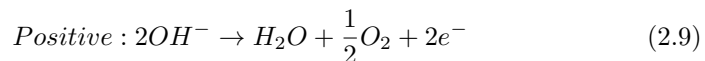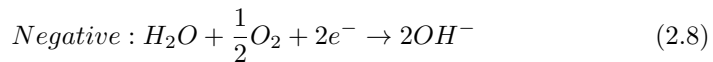
The cell pressure is limited to 1 bar because the cells are open. This limits the property of the metal hydride so that the plateau pressure has to be below 1 bar. Other preferred properties for battery materials are large capacity, good kinetics, small hysteresis, low cost and a high cyclic stability.

2.2.1 Alloy types in NiMH batteries

Currently, AB_5 and AB_2 alloys are used as positive electrode in commercial battery cells. The AB_5 alloys are often intermetallic compound consisting of $LaNi_5$ with some substitutional elements for both the La and the Ni, and an example of a commercial metal hydride for batteries is $MmNi_{3.55}Co_{0.75}Mn_{0.4}Al_{0.3}$ [11]. The AB_2 alloys are often a compound of Zr-Ti-V [12, 13].

2.3 The La-Mg-Ni system

2.3.1 The La-Ni system

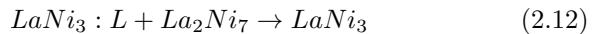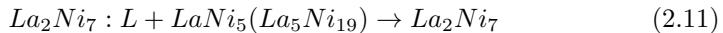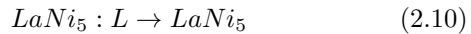Below, in Figure 2.3, the binary phase diagram is shown for the La-Ni system. Important factors here are what kind of reactions demanded to get the different phases. The most important reactions for this work are given in Equation 2.10-2.12.

$$LaNi_5 : L \rightarrow LaNi_5 \tag{2.10}$$
$$La_2Ni_7 : L + LaNi_5(La_5Ni_{19}) \rightarrow La_2Ni_7 \tag{2.11}$$
$$LaNi_3 : L + La_2Ni_7 \rightarrow LaNi_3 \tag{2.12}$$

The type of reactions are very important during solidification. LaNi$_5$ is a congruently melting phase, this means that the phase can be formed directly from a liquid of the correct composition. This makes it fairly easy to form the phase, and the formation is dependent on the rate of nucleation. This phase can be formed at several temperatures and over time. For the LaNi$_3$ and La$_2$Ni$_7$, the reactions making these phases are peritectic. This means that a reaction between the liquid phase of correct composition and a solidified phase has to occur. This property means that the place where this reaction occurs is only on a solid-liquid interface during the solidification of the material and the reaction is therefore more dependent on diffusion. The creation of pure single-phase peritectic compounds is therefore normally a process demanding a rather lengthy annealing process. The corresponding phases in the ternary La-Mg-Ni-system are of the same type as for the La-Ni-system.

2.3.2 AB$_3$ and A$_2$B$_7$ alloys

Due to the relatively low hydrogen storage capacity of the commercial AB$_5$ alloys (280-320mAhg^{-1}) [16], and the high price and difficult activation of the commercial AB$_2$ alloys [13], researchers have been trying to find alternative solutions. New alloys should have the properties listed in the end of Section 2.2. A combination of AB$_5$- and AB$_2$-alloys results in the novel AB$_3$- and A$_2$B$_7$-alloys for the La-Mg-Ni system. Recently, much interest is put on RE-Mg-Ni-based alloys because of their lower densities than the LaNi$_5$-alloys and high reported electrochemical discharge capacity of more than 400mAhg^{-1} [17, 18]. These alloys, however, show a poor cyclic stability and have a low cycle life [18, 19, 20].

(a) Phase diagram for the binary La-Ni system [14].

(b) Close up of the Ni rich part of the La-Ni system [15].

Figure 2.3: *Phase diagrams for the La-Ni system with close up of the Ni-rich part of the system.*

The AB_3 and A_2B_7-alloys are chosen in the RE-Mg-Ni-system due to the high solid solubility of Mg in the structures [1]. These phases have been reported to reach compositions of $LaMg_2Ni_9$ and $La_{1.5}Mg_{0.5}Ni_7$. This is evident from Figure 2.4, which presents an isothermal section of the $Ni-LaNi_2-MgNi_2$-system at $500°C$. This shows the possibility of producing a single-phase compound at proper conditions. A single-phase compound, however, has been very hard to synthesize in practice and usually demands a long annealing time at a high temperature.

2.3.3 Magnesium as addition

The use of magnesium in hydrogen storage applications is motivated by its high hydrogen storage capacity as a pure compound (nominally 7.6 wt%). It is also an inexpensive and readily available element. However, the magnesium hydride formation, as given in Equation 2.13, has been reported [21] to have a rather high enthalpy and entropy of formation and decomposition.

Figure 2.4: *Isothermal section of the Ni-MgNi$_2$-LaNi$_2$ phase diagram at 500 °C [1].*

$$MgH_2 \rightarrow Mg + H_2 \qquad (2.13)$$

$$\Delta H = -74\frac{kJ}{moleH_2} \qquad (2.14)$$

$$\Delta S = -135\frac{J}{KmoleH_2} \qquad (2.15)$$

This, combined with very slow kinetics of dehydrogenation/hydrogenation, results in very high requirements for the working temperature (350-400°C), which makes the material difficult to use as a reversible hydride. These problems may be resolved if Mg is combined with other elements. In alloys of RE-Mg-Ni type, magnesium has an effect of reducing the degree of amorphization of the hydrides [22], decreasing the price of the alloys, increasing the capacity [17, 18] and decreasing the unit cell volume due to its size [2]. Too much magnesium may lead to poor cyclic stability as magnesium can lead to more serious corrosion and pulverization during cycling [23].

2.3.4   Phases in the La-Mg-Ni-system

From earlier work done in the field of La-Mg-Ni crystal structures [2, 17, 22, 24, 25, 26], a number of phases are known in the Ni rich part of the La-Mg-Ni system. These phases are built up of LaNi$_5$- and (La,Mg)$_2$Ni$_4$-type cells stacked in different sequences. The possible phases are a result of Equation 2.16, where the formula is expressing the different ways of stacking the two cell types.

$$AB_y, y = \frac{(5n+4)}{n+2} \tag{2.16}$$

This gives the possible phases given in Table 2.1.

**Table 2.1:** *Phases in the La-Mg-Ni system between the AB$_2$ and AB$_5$ phases after Equation 2.16.*

n	Phase	Multiple stacking	Space group
0	AB$_2$	no	F$\bar{4}$3m
1	AB$_3$	yes	R$\bar{3}$m & P6$_3$/mmc
2	A$_2$B$_7$	yes	R$\bar{3}$m & P6$_3$/mmc
3	A$_5$B$_{19}$	yes	R$\bar{3}$m & P6$_3$/mmc
4	A$_6$B$_{24}$	yes	R$\bar{3}$m & P6$_3$/mmc
∞	AB$_5$	no	P6/mmm

The large unit cells of the mixed structures have a low symmetry and are hard to refine in XRD data. An example of such a structure is shown in Figure 2.5. The Mg in the structures is known to only be in the (La,Mg)$_2$Ni$_4$ Laves type layers [27], and this is important for the Rietveld analysis as described in Section 3.3.2. This is also key in identifying the Mg-free phase LaNi$_5$ during the EDX analysis.

2.4   Solidification

2.4.1   Homogeneous Nucleation

For very quick cooling and high purity of the liquid phase, one may obtain homogeneous nucleation in a supercooled melt. Homogeneous nucleation is the process where a first order transformation between two phases happens spontaneously.
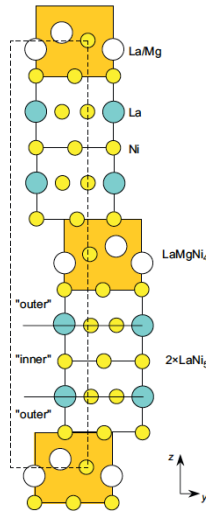
Figure 2.5: *The phase structure of the La_3MgNi_{14}-3R phase as presented by Denys et al [22].*

The equation for steady-state homogeneous nucleation with temperature independent ΔH and ΔS is given in Equation 2.17-2.18 [28].

$$J = J_0 exp(-A(\frac{T_f}{T_f - T})^2) \tag{2.17}$$

$$A = \frac{16\pi}{3} \frac{\nu_s^2 \sigma_{sl}^3}{k_B T (\Delta h_{sl})^2} \tag{2.18}$$

Here, J is the flux of growth of a cluster of size i to size $i+1$, J_0 is a constant, T_f is the equilibrium transformation temperature, and T is the temperature of the material. As is shown here, the primary driving force of the nucleation is the difference in temperature from the transformation temperature. A higher difference in these temperatures will therefore lead to a higher possibility of the growth of large enough clusters leading to solidification. However, for most conditions, the main nucleation mechanism is heterogeneous nucleation. This mechanism does not demand as large temperature difference as homogeneous nucleation since the transformation instead occurs due to the presence of surfaces of other materials or impurities in the mixture. This is a far more common situation. For heterogeneous nucleation, the theoretical treatment of the process is also much more

13

complex.

2.4.2   Rapid Solidification

Rapid solidification (RS) is a technique for rapid quenching of the alloys. There are several techniques designed to obtain high cooling rates of 10^3-10^7K/s. These methods can be classified in the atomization methods, including gas atomization, and chilling methods, including melt spinning (MS). All methods have in common that at least one physical dimension of the rapidly solidified material is small and that the cooling rate is substantially larger than during a conventional casting.

All types of RS techniques show a large grain refinement due to the process. This is because of the possibility of copious heterogeneous nucleation [29]. In melt spinning, the heterogeneous nucleation takes place due to the large contact area between a copper block and the alloy. Here, as the thickness of the sample shrinks due to higher spinning speed, the fraction of heterogeneous nucleation is expected to rise. The melt spinning process can achieve solidification rates of 10^5-10^7 K/s depending mainly on the speed of the wheel and the diameter of crucible hole [30]. Other factors influencing the cooling rate are the thermal conductivities of the cast/wheel interface, the wheel material and the processing inert gas.

Rapid solidification is applied in order to achieve nano-structuring of the alloy. RS leads to grain refinement and in some cases also to more homogeneous alloys, meaning that the resulting phases may be fewer, but not necessarily the equilibrium ones. If very high solidification rates are applied, the technique may lead to amorphization of the alloy.

A fast cooling rate such as that obtained by melt spinning may lead to different phase morphologies. Cooling on a copper wheel would at low solidification front velocities be expected to lead to a planar solidification front. However, with fast cooling, such a front may break down and give cellular or dendritic growth. This is dependent on the two factors solidification front velocity and the parameter d/λ, where d is the secondary dendrite arm spacing and λ is the interfiber spacing. A sketch of the dependence of this is shown in Figure 2.6. For the purpose of this work, the propagation type of the front is dependent on the solidification front velocity.

Earlier work on rapid solidification of hydrogen storage alloys suggests that the technique of melt spinning gives the alloys a flatter PCT plateau and better cyclic stability [32].
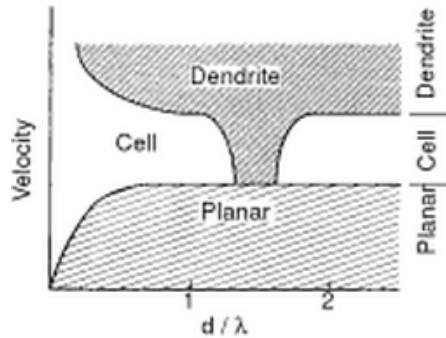
Figure 2.6: *A sketch illustrating the breakdown of planar solidification due to high solidification front velocities [31].*

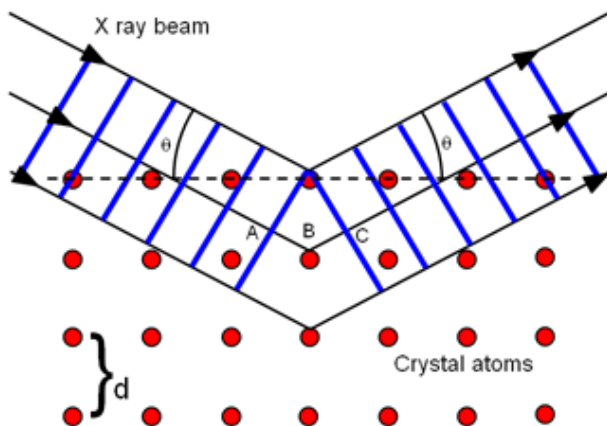## 2.5 X-Ray Diffraction (XRD) measurements

2.5.1 Theory of X-Ray Diffraction measurements

X-ray diffraction (XRD) is a method where the a X-ray beam hits a crystal structure and causes the elastic scattering of the rays in specific directions. The data obtained is a spectrum over a certain range of θ-values as shown the Figures 4.2 & 4.3. The intensities of the peaks in such a spectrum can be used for finding the crystal structure of the material under study. Bragg's law [33], Equation 2.19 illustrated in Figure 2.7, is a simple way to understand the principle of the peaks corresponding to a special set of planes in the structure. Here, d is the spacing between diffracting planes, θ is the incident beam angle, n is any integer, and λ is the wavelength of the beam. A given plane distance, d, will here give a constructive interference at a given angle, θ. Bragg's law, however, does not account for the different in intensities of the reflections collected and therefore, the scattering has to be treated by a Fourier transform method to obtain the necessary information to find the crystal structure. The theoretical treatment of this will not be gone through in this work. The resulting peak intensities are dependent on several factors, including atom type, plane densities, strain rate in crystals and crystallite sizes.

$$n\lambda = 2dsin\theta \qquad (2.19)$$

XRD is only possible if the wavelength of the radiation and the spacing between

15

the atoms are similar in size. It is then possible only for crystalline phases as these have a repetitive order of the atoms giving high intensity reflections. An amorphous structure does not show this and gives instead a diffuse diffraction pattern either as an increased background radiation or show the peaks as hills.

Figure 2.7: *X-ray diffraction in atomic layers in a crystal structure.*

2.5.2 Advantages of Synchrotron X-ray Diffraction (SR-XRD)

Synchrotron X-Ray Diffraction (SR-XRD) measurement differs from conventional XRD measurements due to the high brilliance of the beam. A synchrotron can produce an X-ray beam that is 10^6 times more intensive than the beam for a conventional X-ray source. This gives an advantage of high sensitivity in the data, and makes it possible to determine phase abundances down to 1 wt%. The synchrotron X-ray radiation is also monochromatic, this ensures narrow diffraction peaks and thus good resolution and high accuracy in the determination of the atomic structures and unit cell parameters.

Chapter 3

Experimental

3.1 Sample preparation

The work done during the autumn project [34] showed that the melt spinning led to loss of considerable amounts of Mg during the melt spin processing. Because of this, the samples used in this work had 0%, 15% or 30% excess Mg added to ensure sufficient available Mg for the stoichiometric phases. The different samples produced are presented in Figure 3.1. Here, all the different synthesize methods used in this work are presented.
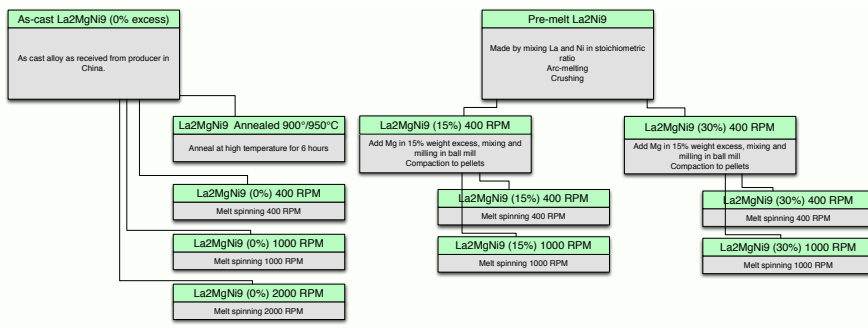
Figure 3.1: *Figure showing the different samples produced and the relation between them.*

The stoichiometric La_2MgNi_9 with no excess Mg were ordered from China and

have been tested to have the required stoichiometric ratio between the elements. The other alloys with excess Mg were produced at IFE by first making pre-melts of La_2Ni_9 composition. These were prepared by Arc-melting in an Edmund Buhler GmbH Arc Melter AM/0.5 and were remelted a total of 5 times to obtain homogeneous alloys. The pre-melts were manually crushed and then brought into a glow box. There, they were packed with a 15% or 30% excess weight amount of magnesium compared to the stoichiometric amount to account for evaporation during the high temperature processing. The Mg was added as powder of less than 300 μm diameter. This mixture was ball-milled with a ball to alloy weight ratio of 6 to 1 in a FRITSCH Pulverisette 6 planetary mill for 1 hour with a rotation speed of 250 RPM. After the ball milling, the mixtures were handled in a glow box and uniaxialy pressed into pellets of approximately 3 grams each. The equipment used is shown in Figure 3.2.

|		
(a) Arc Melter.	(b) Planetary Ball Mill.	(c) Uniaxial Press.
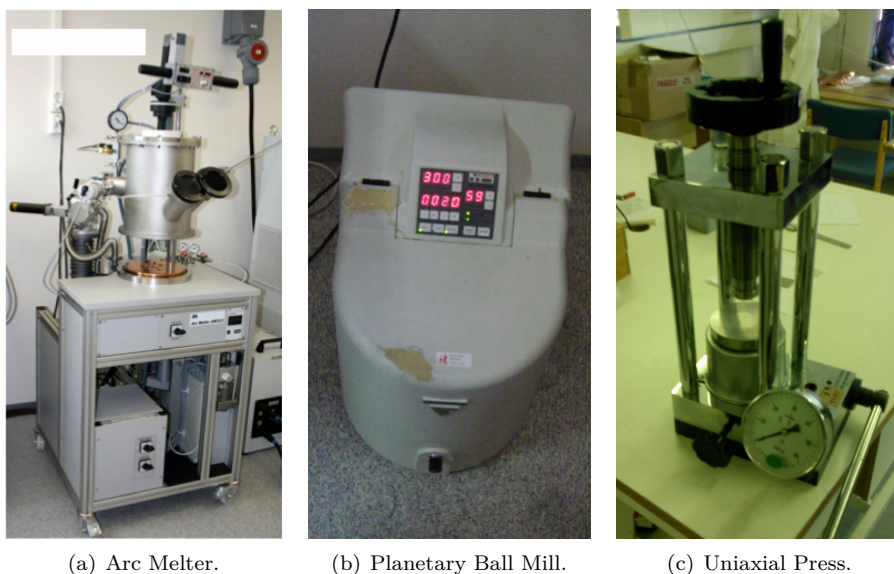
Figure 3.2: *Figure showing the equipment used to make the alloy samples a) Arc Melter, b) Planetary Ball Mill and c) Uniaxial Press.*

The sample with 0% excess Mg was annealed to get the equilibrium phases. This was done by heating the sample first to 500°C, keeping it there for 10-14 hours, then increasing the temperature stepwise to the desired temperature of either 900°C or 950°C. The sample was kept at this temperature for 6 hours, then cooled down to 800°C and kept there for 24 hours. After this, the sample was quenched in water to room temperature. All of this processing was done in a

stainless steel autoclave in Ar atmosphere.

3.2 Rapid solidification
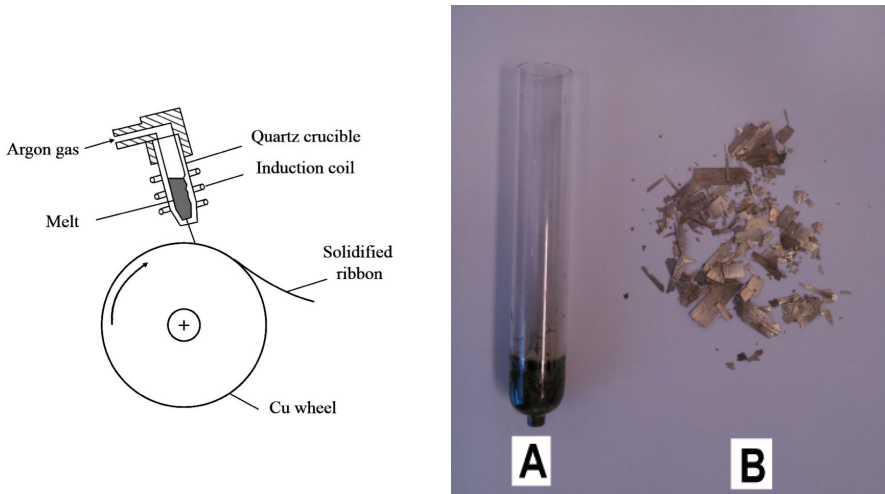
(a) Sketch of the Melt spinning mechanism.

(b) The alloy after melt spinning, A) Quartz cruscible, B) ribbons after melt spinning.

Figure 3.3: *a) Sketch of the melt spinning equipment, b) the quartz cruscible used at NTNU along with an example of the powder produced.*

The samples were rapidly solidified in the melt spinner at NTNU. An example of the setup and the ribbons produced is shown in Figure 3.3. The amount of the sample for each melt spinning experiment varied from about 3 to 8 grams. The samples were melt spun at 0.5 bar Ar pressure and had a distance of about 2 cm from the sample to the wheel with a crucible hole about 3 mm in diameter. The samples used 6% of the power in the power generator for the melt spinner at NTNU. When run, the power was on until the sample visually melted. Over-pressure was applied to push out the melted sample, but this overpressure was normally not necessary as the samples went through the crucible opening themselves when melted. The samples were later collected from below the copper wheel. The spinning speeds used were 400, 1000 and 2000 RPM, corresponding to a wheel rotation speed of 4.2, 10.5 and 20.9 m/s. During earlier work [35], the spin rate vs cooling rate was measured for the wheel and equipment used in this work. The results are shown in Table 3.1.

Table 3.1: *Correlation of wheel spin speed and cooling rates for the equipment at NTNU [35]. Results are for a Mm(Ni,Co,Mn,Al)$_5$-alloy.*

| Spin rate [RPM]	Surface velocity [ms^{-1}]	Atmospheric gas	Cooling rate during solidification [Ks^{-1}]	Cooling rate solid state [Ks^{-1}]
300	3.3	Argon	8.2*10^3	Not measured
800	8.4	Argon	6.1*10^4	1.4*10^5
1000	10.5	Argon	1.6*10^5	2.6*10^5
1500	15.7	Argon	2.8*10^5	4.4*10^5
2000	20.9	Argon	2.8*10^5	Not measured

3.3 X-Ray Diffraction Studies

X-ray Diffraction studies were done at several places. Firstly, all the in situ studies along with all the results for the 0% excess Mg alloys were collected at the European Synchrotron Radiation Facility (ESRF) in Grenoble in September 2011. They were done at a Beam line, BM1B, at the Swiss-Norwegian Beam Lines (SNBL). For the 15% and 30% excess Mg alloys, the data were collected at UiO, done by Per Fostervoll. The instrument at UiO is a BRUKER D8 DISCOVER with Ge-monochromator and a LYNX-Eye detector using the wavelength of Cu-Kα1, where $\lambda = 1.5406$ A.

3.3.1 Setup for Synchrotron Radiation XRD

For ex-situ X-ray study, the melt-spun samples were manually crushed to a powder. This powder was entered into a glass capillary of 0.3 mm outer diameter and mounted to a goniometer's head.

In the ex-situ experiments, the measured 2θ-angles were from 3 to 40 degrees and the wavelength used was $\lambda = 0.5023$ A. The step size was 0.004 degrees and the data collection time was 200 ms pr step. The samples were rotated during the experiment, this was done to average the orientation of the powder particles. The setup of the measurements is shown in Figure 3.4.

For the collection of the in situ data, the samples were manually crushed to powder similarly to the ex-situ preparation. The sample was put in 0.5 mm glass capillary and afterwards put inside a 0.7 mm quartz capillary and mounted to a specially modified goniometer. This setup allowed for changing both the
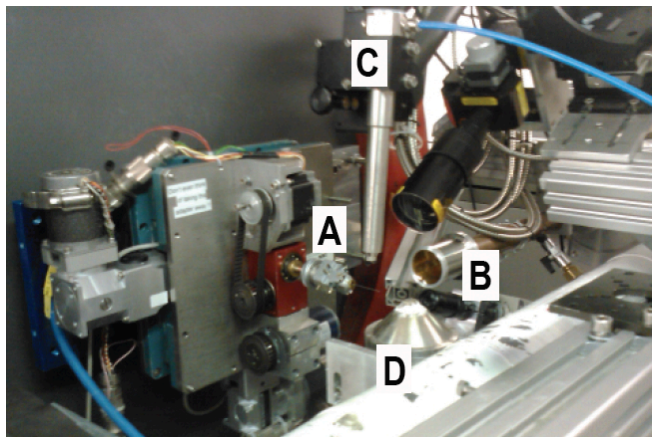
Figure 3.4: *The setup at beam line BM1B at SNBL ESRF used for the ex-situ XRD. A - above goniometer holding the capillary with sample, B - X-ray beam guide, C - combined cryogenic/heating apparatus, D - heating apparatus.*

temperature and pressure during the runs. The pressure set is not dependent on the charge capacity of the sample since the volume with hydrogen is so much bigger than the sample volume. This setup is shown in Figure 3.5.
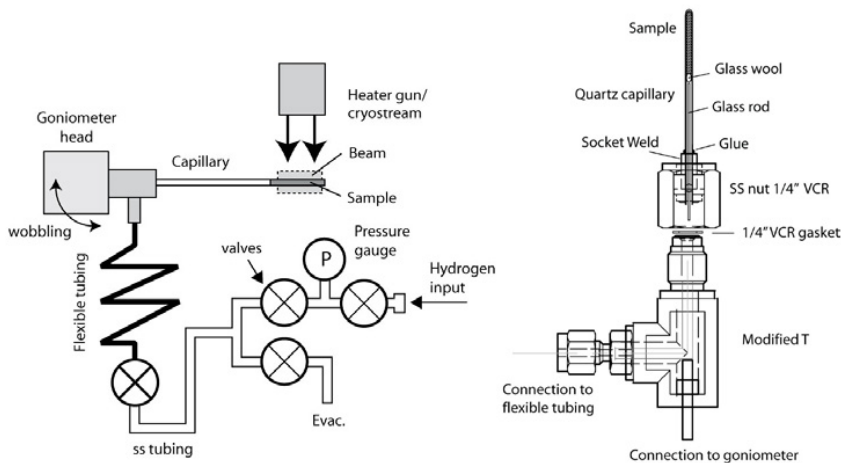
Figure 3.5: *Sketch of the setup for hydrogenation with in-situ XRD.*

3.3.2 Data analysis

The X-ray data were analyzed by using a Rietveld type software package GSAS, which used the least-square approximations. The phases included were the following: (i)La_2MgNi_9, (ii)La_3MgNi_{14}-3R, (iii)$LaNi_5$, (iv)La_4MgNi_{19}- (a)3R & (b)2H, (v)$LaMgNi_4$ and (vi)pure Ni. The data were refined using the following routine:

1. Add the first three phases and adjust the cell parameters and quantities to fit well at a range of the low angle-peaks;

2. Refine the cell parameters, amounts and strain rate in the cells to get a good starting fit;

3. If these phases clearly do not give a very good fit, add the other three phases and check these accordingly and adjust cell parameters to get a good fit;

4. Run refinements again, the phases with a very low abundance in the sample are removed;

5. Use the remaining phases and adjust the background and the displacement parameter (U_{iso})(which was always refined as a group for each phase).

This procedure has given the results given in Section 4.1.

This type of refinements results in a typical fit as shown in Figure 3.6. This plot shows the sample La_2MgNi_9 with 1000 RPM spin rate. In the figure, the observed data is overlapped by the calculated data (red line), and the mismatch between these two datasets is shown as the diff (blue line). The phases in the example are the phases $LaNi_5$ (pink), La_2MgNi_9 (light blue), La_3MgNi_{14}-3R (black) and $LaMgNi_4$ (brown).

For the in-situ data, a long scan was performed so all of the steps above could be used to refine the data. After that, the phase information given from the good scan was used for the in-situ data to get a good starting fit for the short time in-situ scans. For the in-situ data, generally only the two first steps were used of the recipe given above for the refinements. These refinements were however very inconclusive due to the low resolution and were mostly used for qualitative analysis.
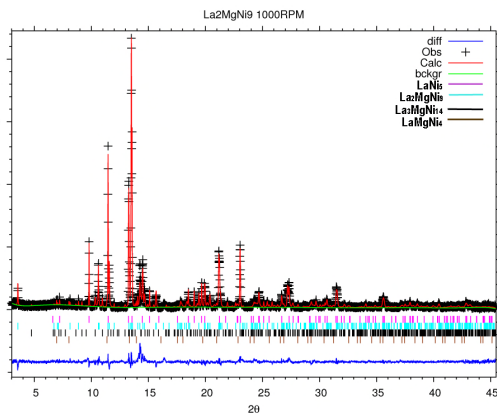
Figure 3.6: *Figure showing the XRD refinement for the sample with no excess Mg melt spun at 1000 RPM. The phases in the example are the phases LaNi$_5$ (pink), La$_2$MgNi$_9$ (light blue), La$_3$MgNi$_{14}$-3R (black) and LaMgNi$_4$ (brown).*
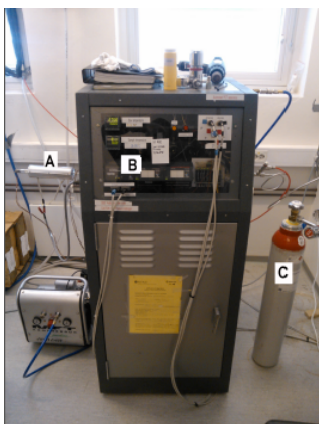
(a) Automatic PCT.
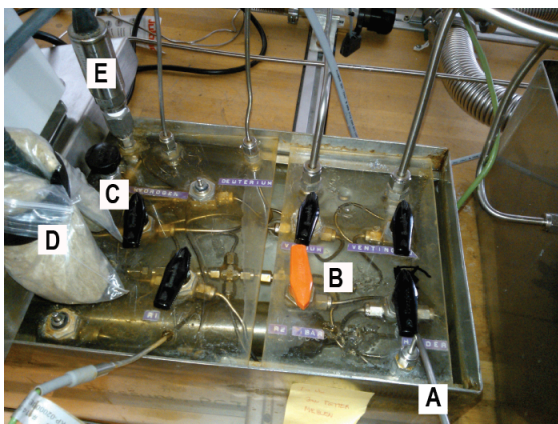
(b) Low pressure PCT setup (0-25 bar).

Figure 3.7: *PCT setup used, a) shows the automatic PCT apparatus, with A - sample holder, B - system volume and C - hydrogen source, while b) shows the low pressure PCT setup with A - tube to sample holder, B - system volume in water tank, C - hydrogen intake, D - low pressure sensor and E - high pressure sensor.*

3.4 Gaseous hydrogen absorption/desorption studies

For the pressure-composition-temperature (PCT) studies, the samples are exposed to gaseous hydrogen. This was done in both in the low-pressure PCT

setup at IFE and at an automatic PCT at IFE. Both of these setups are shown in Figure 3.7, and they are both Sieverts type apparatus based on calculating the hydrogen absorption/desorption by measuring the pressure difference on a known volume with a controlled temperature. In the low pressure setup, two pressure sensors were used; one from 0-1 bar and one from 1-25 bar. The temperature was measured at three points; in the bath, in the room and at the sample. For the automatic PCT setup, there were two sensors as well; the low pressure sensor was used from 1-5 bar, while the high pressure sensor was used from 5-50 bar. The temperature was here measured in the box room (where most of the volumes were), and at the sample.

Due to problems with capacity loss in the samples after cycling in PCT, a procedure for regeneration of the samples was applied. This consisted of heating the samples under high vacuum. First, a high vacuum was obtained in room temperature, then the sample was heated to get complete desorption. The temperature used was up to 450°C. The sample was under constant vacuum during the whole process, but a vacuum sensor was used to give an indication of the rate of desorption.
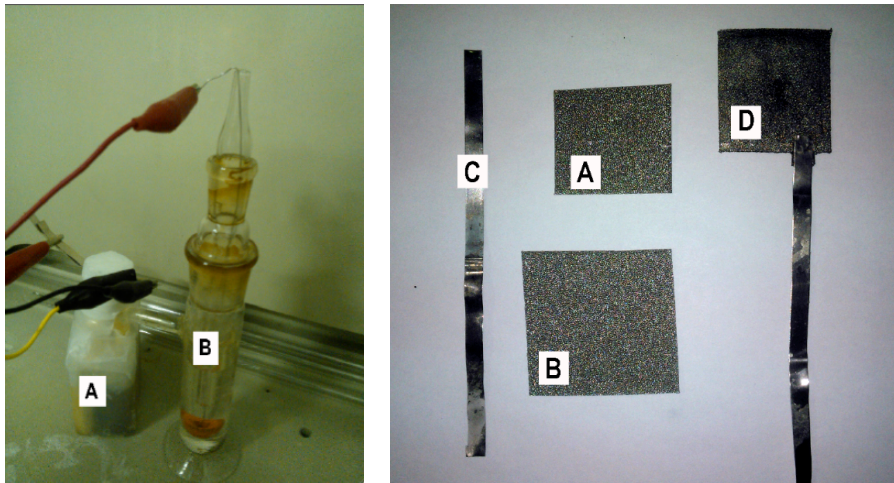
3.5 Electrochemical Testing

3.5.1 Sample preparation

The samples for electrochemical testing were crushed into fine powder and sieved to separate a fraction between mesh 200 and 360 (size 40-61 μm). This powder was weighted to 0.667 gram and mixed with 0.067 gram of carbon powder. A small amount of binder (PTFE) was also added to the mixture. This mixture was then spread evenly on a nickel sponge of size 3.0 by 3.2 cm and a similar nickel sponge was added above. These were welded to contacts and pressed together. This whole square piece was then put in a polymer membrane and put in the setup as shown in Figure 3.8. The counter electrode was a NiOOH electrode of slightly larger size than the working electrode and the electrolyte was a 9M KOH. The reference electrode was a Hg/HgO electrode. The whole setup was left for 18 hours to settle before current was applied.

3.5.2 Testing setup

The current applied was 19 mA, which for our sample corresponded to about 24 mA/g. This should correspond to a discharge current of about 0.1C (One

(a) Setup for electrochemical measurement.

(b) The Ni sponge used as electrode material, a Ni ribbon used for electronic contact and a complete metal hydride electrode.

Figure 3.8: *Setup used for electrochemical testing showing in a) the cell (A) and Hg/HgO reference electrode (B), b) shows the two Nickel sponges used for covering the metal hydride powder (A and B) and the Ni ribbon used for electronic contact (C), along with an example of a complete metal hydride electrode (D).*

discharge cycle in 10 hours).

3.6 Scanning Electron Microscopy (SEM)

3.6.1 Sample preparation for SEM

The samples were prepared for SEM by casting them into a conductive polymer. They were ground and polished down to 1 μm. The cross section was the main area of focus.

3.6.2 SEM conditions

The SEM study was done using a Zeiss Supra 55VP, LVSEM. Recommended settings for the Zeiss Supra is to use large aperture (120 or $300\mu m$), high current

mode and to use the backscatter detector to get good contrast. This is due to the small grain size of the phases in the samples.
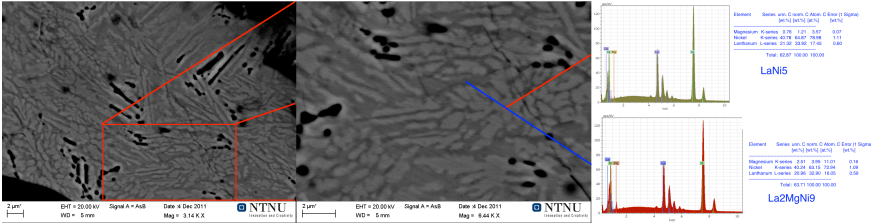
Figure 3.9: *Example of EDX mapping of the 0% excess Mg sample melt spun at 2000 RPM, showing the spectra and quantitative analysis.*

Built-in electron dispersive X-ray spectroscopy (EDX) detector is available in the Zeiss Supra 55VP and was extensively used. The EDX detector was a Bruker AXS EDX detector using ESPRIT software. The EDX detector was used for phase identification. This worked fine for larger phase areas at low spin rates. For phases produced at the high spin rates, the phases were often less than $1\,\mu m$ in diameter, and the emission volume for the X-rays may be larger than the phases. This may give some distortion from nearby phases in the spectra. There were also some problems with the drift in the images and this was solved by having relatively short data collection time (30 s) for the EDX spectra to make sure it still was in the right phase during the whole scan.

The data from the EDX detector can be used for the phase identification. In Figure 3.9, the use of the technique is shown for the La_2MgNi_9 alloy at 2000 RPM spin rate. The image is here first used to identify large phase areas. Thereafter, a scan is run for the chosen areas, and the quantitative data is compared with the phase composition from the X-ray Diffraction data. These two analyses together provides the basis for how to identify the phases in the images. This is important as the EDX data are not completely accurate for the reasons stated in the above paragraph.

Chapter 4

Results

4.1 X-Ray Diffraction

4.1.1 Refinements for the ex-situ data

All samples were investigated by X-Ray Diffraction, and the samples with 0% excess Mg were measured using synchrotron radiation, while the alloys with 15% and 30% excess were measured with conventional X-rays. An example of such a refinement is shown in Figure 3.6. The unit cell sizes along with weight fractions of the phases are shown in Figure 4.1, these values are shown in more detail in Tables 4.1-4.3. For all these samples, the main constituents are the phases La_2MgNi_9, $LaNi_5$ and La_3MgNi_{14}.

Figure 4.2 shows the XRD patterns for the rapidly solidified phases. By comparing the relative peak intensities, one can see that the amount of $LaNi_5$ changes due to the conditions applied. As shown by the Rietveld analysis, the 30% excess Mg sample melt spun at 400 RPM is the sample with the largest amount of useful phases (La_2MgNi_9 and La_3MgNi_{14}) with a total amount of 85 wt%. In figure 4.3, the best phase in the XRD data, the 30% excess Mg sample spun at 400 RPM, is compared with the 0% excess sample as-cast and a 0% excess Mg sample annealed at 950°C sample. From this figure it is clear that the 30% excess Mg sample at 400 RPM is considerably closer to single phase than the as-cast sample for 0% excess. However, it is not as good as the annealed sample, since this sample consists of only the La_2MgNi_9 and La_3MgNi_{14} phases, while the melt spun sample still contains some $LaNi_5$ phase.
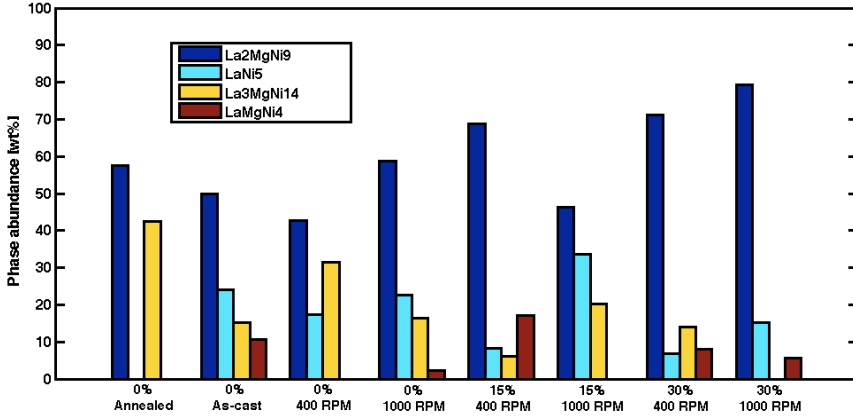
Figure 4.1: *Figure showing the weight fractions of the phases vs the conditions applied.*

Table 4.1: *The cell parameters and weight fractions of the La_2MgNi_9 0% excess Mg samples. The standard deviation is shown in parenthesis after the numbers.*

Sample	Phase	Wt%	a [A]	c [A]	Vol [A^3]
As-cast	La_2MgNi_9	50.0(3)	5.0390(2)	24.326(1)	534.92(4)
	$LaNi_5$	24.1(2)	5.0357(2)	3.9941(2)	87.713(6)
	La_3MgNi_{14}	15.3(3)	5.0375(4)	36.270(4)	797.1(1)
	$LaMgNi_4$	10.6(2)	7.1778(2)	7.1778(2)	369.81(4)
400 RPM	La_2MgNi_9	42.8(3)	5.0321(2)	24.310(2)	533.12(5)
	$LaNi_5$	17.3(2)	5.0266(2)	3.9877(2)	87.258(6)
	La_3MgNi_{14}	31.5(4)	5.0284(2)	36.218(2)	793.08(6)
	La_4MgNi_{19}	8.5(3)	5.0265(6)	48.233(7)	1055.4(2)
1000 RPM	La_2MgNi_9	58.7(4)	5.0322(2)	24.292(2)	532.74(5)
	$LaNi_5$	22.6(4)	5.0246(2)	3.9893(3)	87.222(8)
	La_3MgNi_{14}	16.4(6)	5.0303(4)	36.251(6)	794.4(2)
	$LaMgNi_4$	2.3(3)	7.1692(9)	7.1692(9)	368.5(1)
2000 RPM	La_2MgNi_9	57.0(3)	5.0332(2)	24.292(1)	532.94(4)
	$LaNi_5$	31.7(3)	5.0223(2)	3.9890(2)	87.139(5)
	La_3MgNi_{14}	4.8(4)	5.027(1)	36.323(8)	794.9(3)
	$LaMgNi_4$	6.5(2)	7.1637(3)	7.1637(3)	367.63(5)
Annealed 950°C	La_2MgNi_9	57.6(3)	5.0375(1)	24.296(1)	533.95(3)
	La_3MgNi_{14}	42.4(3)	5.0406(1)	36.327(2)	799.33(5)
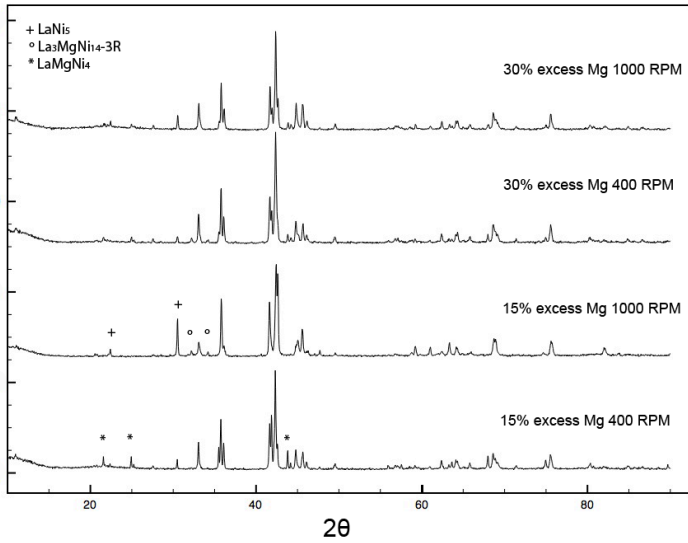
Figure 4.2: *XRD patterns showing the peaks of the 15% exccess and 30% excess Mg samples.*
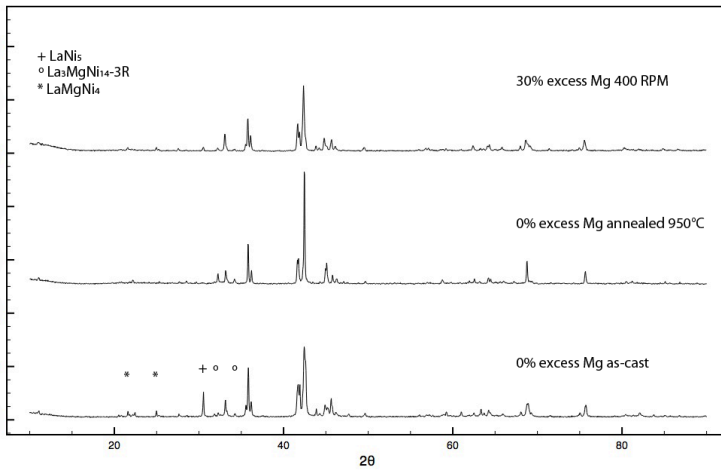
Figure 4.3: *XRD patterns for the as-cast and annealed at 950° C sample compared with the best melt spun sample at 30% excess Mg and 400 RPM spin rate.*

Table 4.2: *The cell parameters and weight fractions of the La_2MgNi_9 15% excess Mg samples. Standard deviation is in parenthesis after the numbers.*

Sample	Phase	Wt%	a [A]	c [A]	Vol [A^3]
400 RPM	La_2MgNi_9	68.7(2)	5.0456(1)	24.3634(8)	537.14(2)
	$LaNi_5$	8.2(2)	5.0365(3)	3.9963(4)	87.79(1)
	La_3MgNi_{14}	6.0(3)	5.040(1)	36.39(1)	800.6(4)
	$LaMgNi_4$	17.0(2)	7.1823(1)	7.1823(1)	370.50(2)
1000 RPM	La_2MgNi_9	46.3(3)	5.0434(3)	24.347(2)	536.31(6)
	$LaNi_5$	33.5(2)	5.0343(1)	3.9962(2)	87.712(5)
	La_3MgNi_{14}	20.3(3)	5.0439(3)	36.359(3)	801.1(1)

Table 4.3: *The cell parameters and weight fractions of the La_2MgNi_9 30% excess Mg samples. Standard deviation in parenthesis after the numbers.*

Sample	Phase	Wt%	a [A]	c [A]	Vol [A^3]
400 RPM	La_2MgNi_9	71.2(1)	5.0466(1)	24.3770(9)	537.66(3)
	$LaNi_5$	6.9(2)	5.0376(4)	3.9964(5)	87.83(2)
	La_3MgNi_{14}	14.0(3)	5.0429(4)	36.357(5)	800.7(1)
	$LaMgNi_4$	7.9(2)	7.1848(2)	7.1848(2)	370.89(4)
1000 RPM	La_2MgNi_9	79.2(1)	5.0464(1)	24.3691(9)	.537.44(3)
	$LaNi_5$	15.2(2)	5.0356(3)	3.9964(4)	87.76(1)
	$LaMgNi_4$	5.6(2)	7.1828(3)	7.1828(3)	370.58(5)

4.1.2 Total phase stoichiometry based on XRD data

In Table 4.4, the total stoichiometry for the samples is shown. This is calculated from the phase abundances from the XRD refinements.

4.1.3 XRD data for the hydrides formed

In-situ XRD was run on the samples with 0% excess Mg melt spun at 1000 and 2000 RPM and the annealed version of this sample at 900°C.

In Table 4.5, the unit cell parameters are shown for the 0% excess Mg alloy at preparation RS 1000 RPM, RS 2000 RPM and annealed sample. As one can see, the formation of hydride normally yields a 25-26% volume expansion. The exception is the 0% excess Mg sample spun at 2000 RPM, this sample has a relatively low volume expansion for the La_2MgNi_9 phase.

**Table 4.4:** *Total sample stoichiometry based on the XRD Rietveld refinements.*

Alloy	Spin rate [RPM]	Total stoichiometry
La$_2$MgNi$_9$+0%	as-cast	La$_{1.96}$Mg$_{0.81}$Ni$_9$
	400	La$_{1.89}$Mg$_{0.70}$Ni$_9$
	1000	La$_{1.93}$Mg$_{0.75}$Ni$_9$
	950°C annealed	La$_{1.97}$Mg$_{0.85}$Ni$_9$
La$_2$MgNi$_9$+15%	400	La$_{2.02}$Mg$_{1.09}$Ni$_9$
	1000	La$_{1.92}$Mg$_{0.58}$Ni$_9$
La$_2$MgNi$_9$+30%	400	La$_{2.01}$Mg$_{0.97}$Ni$_9$
	1000	La$_{1.86}$Mg$_{0.84}$Ni$_9$

Table 4.5: *The cell parameters and weight fractions of the hydrogenated La$_2$MgNi$_9$ 0% excess Mg samples. The standard deviation is shown in parenthesis after the numbers.*

Sample	Phase	Wt%	a [A]	c [A]	Vol [A^3]	$\frac{\Delta V}{V}$
1000 RPM	La$_2$MgNi$_9$	30.3(4)	5.4086(5)	26.427(3)	669.51(8)	0.257
	LaNi$_5$	19.7(2)	5.4145(3)	4.3118(3)	109.475(9)	0.255
	La$_3$MgNi$_{14}$	50.0(9)	5.413(1)	39.300(9)	997.4(3)	0.256
2000 RPM	La$_2$MgNi$_9$	57.4(5)	5.220(4)	24.46(4)	577(1)	0.083
	LaNi$_5$	19.6(3)	5.386(2)	4.303(2)	108.11(8)	0.241
	La$_3$MgNi$_{14}$	23.0(6)	5.324(2)	39.98(3)	982(1)	0.235
Annealed	La$_2$MgNi$_9$	46.0(3)	5.3914(3)	26.476(2)	666.48(9)	0.255
	La$_3$MgNi$_{14}$	23.4(5)	5.4178(4)	39.348(3)	1000.2(1)	0.258
	La$_4$MgNi$_{19}$	18.9(4)	5.4120(5)	52.583(6)	1333.8(2)	0.260

4.1.4 XRD data for the hydrogenated samples

In Figure 4.4, the XRD plots are shown for a selection of the samples from before hydrogenation and after 5 cycles of hydrogenation and dehydrogenation. As can be seen from the figure, the samples show a large decrease in intensity and a large degree of amorphization, evidenced by the presence of broad diffuse peaks at 2Θ angles of 22° and 42°. The remaining peaks in the figures after hydrogenation correspond well to the LaNi$_5$ phase. The peaks corresponding to La$_2$MgNi$_9$ and La$_3$MgNi$_{14}$ phase have mostly disappeared, and the peak intensities of the resulting plot is very dependent on the amount of LaNi$_5$ phase in the original sample. For this reason, the method described in the end of Section 3.4 was tried in order to recover the samples into the original form.

(a) 15% excess Mg at 1000 RPM.

(b) 30% excess Mg at 400 RPM.

(c) 30% excess Mg at 1000 RPM.
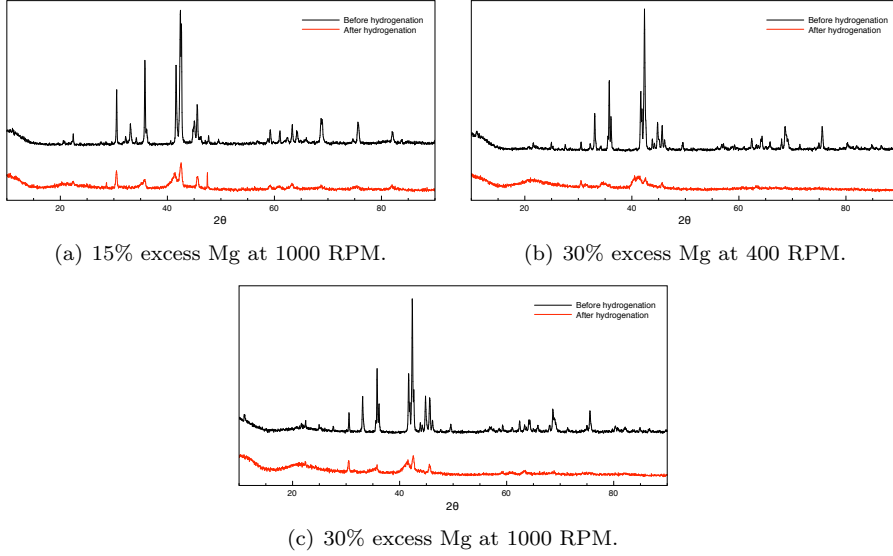
Figure 4.4: *XRD plots for the samples before any hydrogenation and after 5 cycles of hydrogenation and dehydrogenation.*

4.1.5 Check for presence of non-stoichiometric LaNi$_5$ phase

It was suspected that the LaNi$_5$ phase formed through the melt spinning may form a non-stoichiometric compound. Based on the unit cell parameters, these were compared to the work by Notten et al [36]. In this work, the deviation from stoichiometry was given with a factor y, as given in Equation 4.1. This factor gives the formula for the phase as A$_{1-y}$B$_{5+2y}$, from the value of x from the formula of AB$_x$.

$$y = \frac{(x-5)}{(x+2)} \tag{4.1}$$

In the work by Notten et al [36], a linear relationship between the a and c value depending on the y was given, and they are presented in Equations 4.2-4.3, where y is given as 100*y.

32

$$a = 5.0155 - 0.0037y \qquad (4.2)$$
$$c = 3.983 + 0.0028y \qquad (4.3)$$

This regularity is not present in the refinements done for the LaNi$_5$ phase found in the samples produced here. All the samples in this work instead have a decrease in the a-value compared to the literature data, and an increase in the c-value. This is shown in Table 4.6, where the y-value calculated for the a and c values are shown for the different samples. Instead of getting a non-stoichiometric phase, the structure seems to be slightly distorted by compressing the a directions and expanding the c direction.

Table 4.6: *Y-values calculated for the different directions for the LaNi$_5$ phase in this work.*

| Alloy	Spin rate [RPM]	Y-value, a-dir	Y-value, c-dir
La$_2$MgNi$_9$+0%	400	-3.0	1.68
	1000	-2.46	2.25
La$_2$MgNi$_9$+15%	400	-5.68	4.75
	1000	-5.08	4.71
La$_2$MgNi$_9$+30%	400	-5.97	4.79
	1000	-5.43	4.79

4.1.6   In-situ data

The in-situ experiments were done with Synchrotron X-ray radiation. The data were not good enough to yield high quality quantitative data for the phase transformations during the heating or cooling of the samples. However, the qualitative difference of transformation temperatures in the phases is visible and is shown in Figures 4.5-4.9.

0% excess Mg sample melt spun at 1000 RPM

Figure 4.5 shows the 0% excess Mg sample spun at 1000 RPM. The sample is shown during heating of the sample under 2 bar of H$_2$-pressure. This condition results in desorption of hydrogen from the sample, where the sample goes from hydrogenated phase at low temperature to a dehydrogenated sample at high
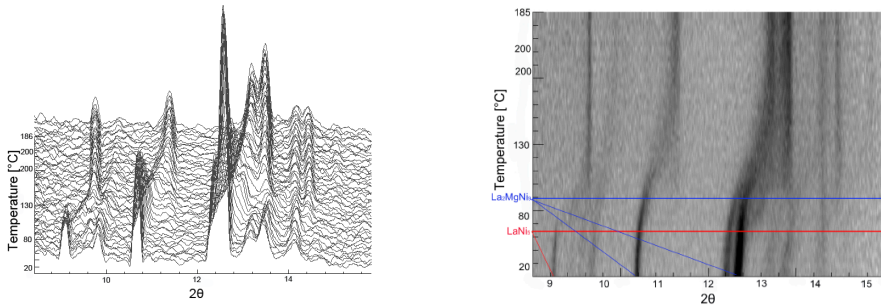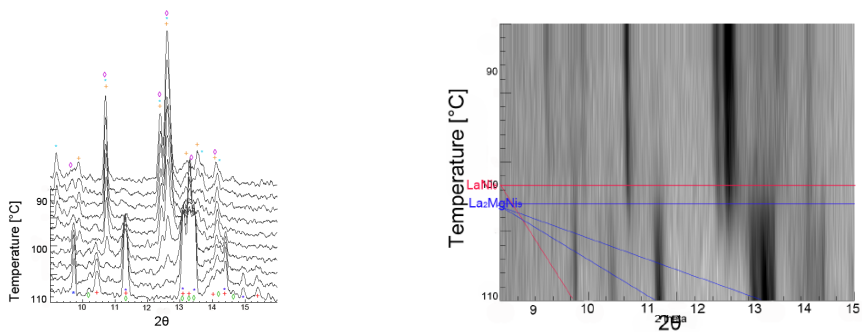
(a) 3D plot of the in situ data for the RS 1000 RPM sample.

(b) 2D plot of the in situ data for the RS 1000 RPM sample. Colored lines indicate the start of transformation.

Figure 4.5: *2D and 3D plot of the XRD patterns during in-situ run for the 0% excess Mg sample at 1000 RPM spin rate during desorption. Temperature scale is linear up to 200° C.*

temperature. As one can see most easily from the 2D plot, Figure 4.5(b), there are clear differences between the transformation temperatures for the different phases. The left peak at $2\Theta = 9$ degrees is a unique $LaNi_5$ peak, and this phase desorbs hydrogen first at about 60°C as indicated by the red line in Figure 4.5(b). This is quite different from the other large peaks that corresponds mostly to the La_2MgNi_9 phase, and this shows a beginning of transformation first at about 100 °C. This is indicated by the blue lines in Figure 4.5(b).

Figure 4.6 shows the 0% excess Mg sample melt spun at 1000 RPM during cooling in 21.4 bar H_2-pressure. This condition results in absorption of hydrogen in the sample, and is a continuation of the process as described for Figure 4.5. As during desorption, shown in Figure 4.5, there are differences in when the phases are being hydrogenated. These differences are not as large as for the sample during desorption, and the complete phase transformation for all the phases occur in a temperature window of about 5K. Although the temperature window of transformation is small, there is a clear difference of transformation temperature where the La_2MgNi_9 phase transforms at a higher temperature, while the $LaNi_5$ is transformed later shown by the longer stretch for the peak at $2\Theta = 9.8°$. This is indicated by the red and blue line in the diagram for the $LaNi_5$ and the La_2MgNi_9 phase respectively.

(a) 3D plot of the in situ data for the RS 1000 RPM sample.

(b) 2D plot of the in situ data for the RS 1000 RPM sample. Colored lines indicate the start of transformation.

Figure 4.6: *2D and 3D plot of the XRD patterns during in-situ run for the 0% excess Mg sample at 1000 RPM spin rate during absorption.*
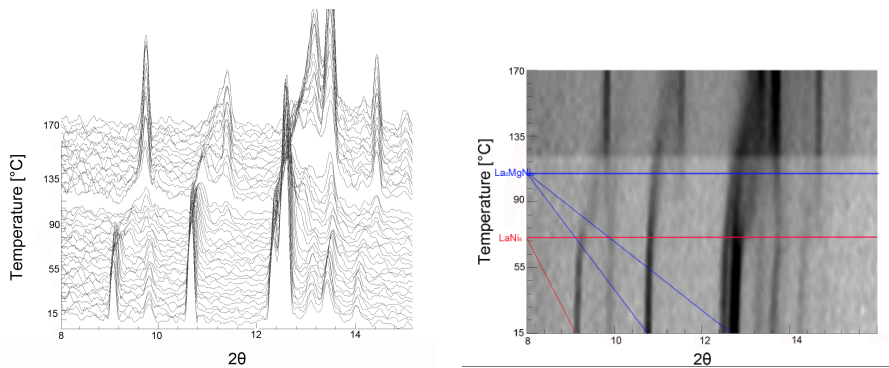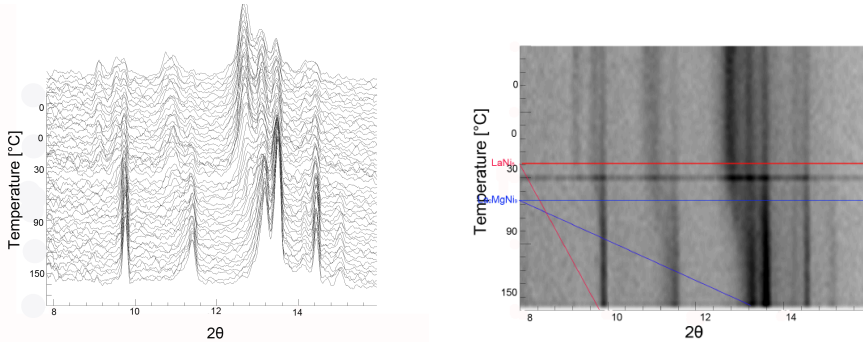

(a) 3D plot of the in situ data for the RS 2000 RPM sample.

(b) 2D plot of the in situ data for the RS 1000 RPM sample. Colored lines indicate the start of transformation.

Figure 4.7: *2D and 3D plot of the XRD patterns during in-situ run for the 0% excess Mg sample at 2000 RPM spin rate during desorption.*

0% excess Mg sample melt spun at 2000 RPM

Figure 4.7 shows the 0% excess Mg sample melt spun at 2000 RPM. This sample was heated in 5 bar H_2-pressure and is therefore desorbing hydrogen. There are clear differences in transformation temperature for the constituent phases. This

35

sample mainly contains the La_2MgNi_9 and the $LaNi_5$ phases and the difference in the temperature at the start of the transformation follows the same pattern as for the samples melt spun at 1000 RPM. This start of transformation is indicated by the red and blue line for the $LaNi_5$ and the La_2MgNi_9 phase respectively.

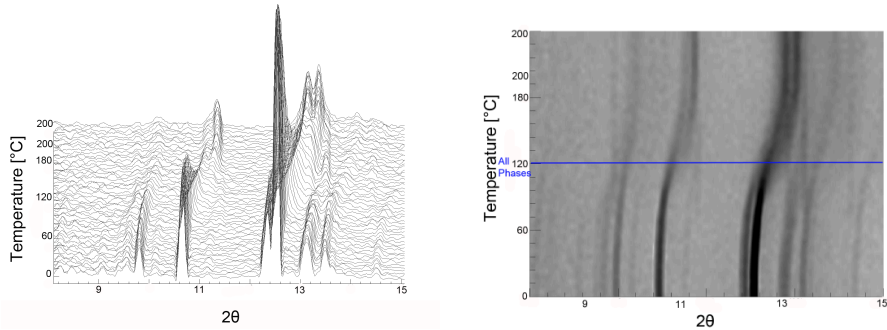(a) 3D plot of the in situ data for the RS 2000 RPM sample.

(b) 2D plot of the in situ data for the RS 1000 RPM sample. Colored lines indicate the start of transformation.

Figure 4.8: *2D and 3D plot of the XRD patterns during in-situ run for the 0% excess Mg sample at 2000 RPM spin rate during absorption. Temperature scale is linear down to 0°C.*

Figure 4.8 shows the 0% excess Mg sample melt spun at 2000 RPM. This sample was cooled in 5 bar H_2-pressure and is absorbing hydrogen. A difference in temperature of transformation between the main phases is again visible. This is indicated by the red and blue line in the figure for the $LaNi_5$ and the La_2MgNi_9 phase respectively. The temperature difference between the transformation temperature is very much smaller for the absorption plot than for the desorption plot as is also visible for the sample spun at 1000 RPM.

0% excess Mg sample annealed at 900°C for 6hrs

Figure 4.9 shows the sample annealed at 900°C for 6 hrs during desorption. The conditions were heating under 5 bar of H_2-pressure, and this results in desorption of H_2 from the sample. This sample is different from the two melt spun samples concerning which phases are present and the phase abundances are close to the values for the sample annealed at 950°C. This value is shown in Table 4.1. Here, very little $LaNi_5$ phase is present in the sample as this sample is mostly consists of La_2MgNi_9 and La_3MgNi_{14} phases. The transformation temperature is therefore similar for all the phases present. This is visible as the blue line in Figure 4.9(b).

(a) 3D plot of the in situ data for the annealed sample.

(b) 2D plot of the in situ data for the annealed sample. Colored line indicate the start of transformation.

Figure 4.9: *2D and 3D plot of the XRD patterns during in-situ run for the annealed 0% excess Mg sample during desorption. Temperature scale is linear up to $200°C$.*

## 4.2 Electrochemical testing

4.2.1 Maximum discharge capacity

The maximum discharge capacity for the tested samples are summed up in Table 4.7. This is the maximum discharge capacity available for the cycles measured and the values were reached during one of the first three cycles.

Table 4.7: *The maximum electrochemical capacity measured for the samples.*

Alloy	Spin rate [RPM]	Max capacity $\left[\frac{mAh}{g}\right]$
La_2MgNi_9+0%Mg	1000	259
	2000	223
La_2MgNi_9+15%Mg	400	290
	1000	271
La_2MgNi_9+30%Mg	400	297
	1000	251

For the best sample, the sample with 30% excess Mg melt spun at 400 RPM, the cyclic stability was measured for 26 cycles. This result is shown in Figure 4.10. As can be seen from this figure, the capacity drops quite fast. The straight blue line in the figure is an extrapolation of the data, this is not the real value for

the capacity drop. The drop is expected to shrink less than the extrapolation indicates.
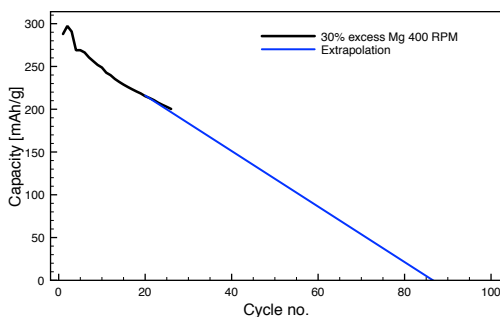

Figure 4.10: *Cycling data for the 30% excess Mg sample spun at 400 RPM, the data are extrapolated after the 26th cycle.*

Plot for the first three cycles for all the measured phases are plotted in Appendix C.

4.3 Pressure-Composition-Temperature diagrams (PCT)

PCT curves were measured for a selection of the samples. These were 15% excess Mg at 1000 RPM, 30% excess Mg at 400 RPM, 30% excess at 1000 RPM and the 0% excess Mg annealed sample at 950°C.

The isotherms for the melt spun alloys are all shown in Figure 4.11, and the figure shows the first cycle and the fourth cycle of the samples, both at 50°C. As can be seen, the maximum hydrogen capacity is similar for all the alloys and is between 1.4 wt% and 1.5 wt%. They also have similar plateau pressures for the first absorption step, which is between 1.5 and 3 bar. After a few cycles, the capacity dropped drastically for all the samples as indicated by the curve for the fourth cycle for all the plots. The curve is also very much steeper than the first cycle. The resulting lowering of capacity due to just a few cycles of hydrogenation and dehydrogenation led to the necessity to do a XRD check of the samples after a few cycles of hydrogenation. This was done, and the result for this is shown in Figure 4.4. This also led to the development of the procedure of regeneration described in the section below.
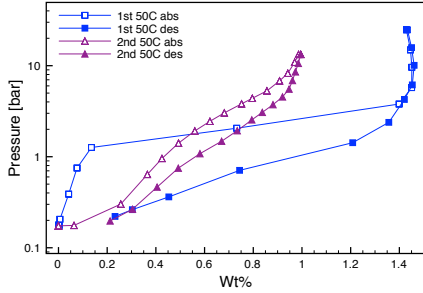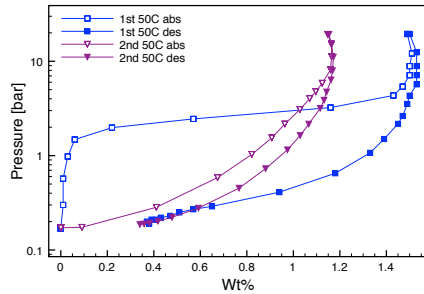
(a) 15% excess Mg at 1000 RPM.
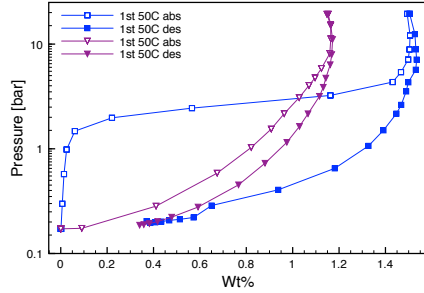
(b) 30% excess Mg at 400 RPM.
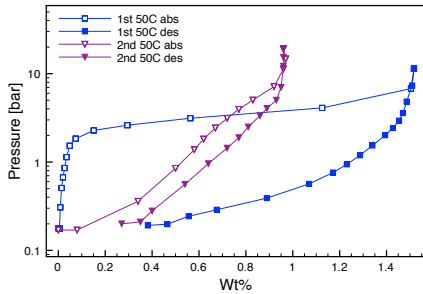
(c) 30% excess Mg at 1000 RPM.

(d) 0% excess Mg annealed at 950°C for 6h.

Figure 4.11: *PCT curves for the melt spun samples, and as can be seen, the capacity is lowered very much after a few cycles. The figures show cycle 1 and cycle 4.*

4.4   Regeneration and stabilization of the phases

The hydride showed poor cyclic stability during hydrogenation and dehydrogenation, as shown in Figures 4.4 & 4.11. An effort was therefore made to regenerate these samples and try to make all of the hydride phases reversible. The testing was done on the 30% excess Mg sample melt spun at 400 RPM and at 1000 RPM. As it was the hydrogenation that caused the amorphization of the samples, the chosen procedure to regenerate the samples was to put the samples under a vacuum sensor and heat the samples in vacuum. The heating of these samples to 400°C yielded a good result as shown in Figure 4.12(a). These results show that through this treatment, the original capacity was obtained. Although the original phase composition could be obtained by this treatment, more PCT cycling again resulted in the lowering of total capacity for the samples similar to what was shown in Figure 4.11.
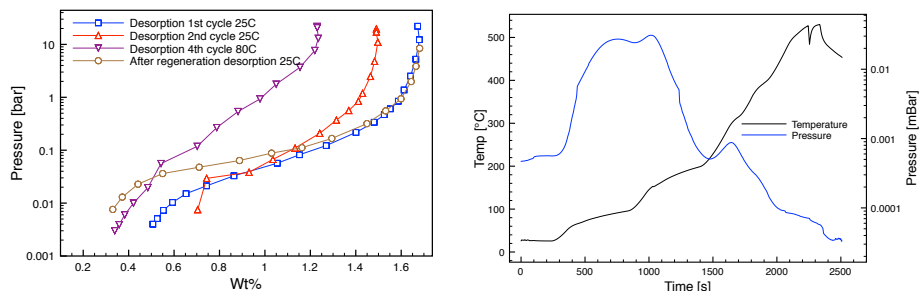
(a) PCT curves for the sample during cycling and showing the retained capacity after regeneration.

(b) The pressure in the vacuum sensor and the temperature during the regeneration process.

Figure 4.12: *PCT and pressure vs temp plot for the 30% excess Mg sample melt spun at 400 RPM.*

For this reason, it was suspected that the sample was amorphisized due to the temperature during the PCT runs. To check for this, a regenerated sample was run at -10°C. The procedure resulted in few results since the low temperature made the plateau pressure during desorption to be below the sensibility of the sensors used.

During regeneration, the samples were put under vacuum with a vacuum sensor, and the temperature and pressure were recorded. This is plotted in Figure 4.12(b) for the sample with 30% excess Mg melt spun at 400 RPM. A higher pressure in this figure indicates desorption and as can be seen, the desorption starts at once as the heating begins. The desorption process is mainly finished at around 200-250°C. At high temperature (400-500°C), the pressure is very low indicating no hydrogen left in the sample.

Figure 4.13 shows the XRD results for the 30% excess Mg sample spun at 1000 RPM. This includes the result before hydrogenation, after hydrogenation and dehydrogenation, and after regeneration. From this, it is visible that the regeneration process is largely successful in bringing back the original peak in the plot. The intensities, however, are not as high as in the original plot.

4.5 Studies by SEM and EDX

Investigation of the samples by SEM and EDX was done by Christopher Nwakwuo at NTNU. The results here are used to confirm or change the results obtained by
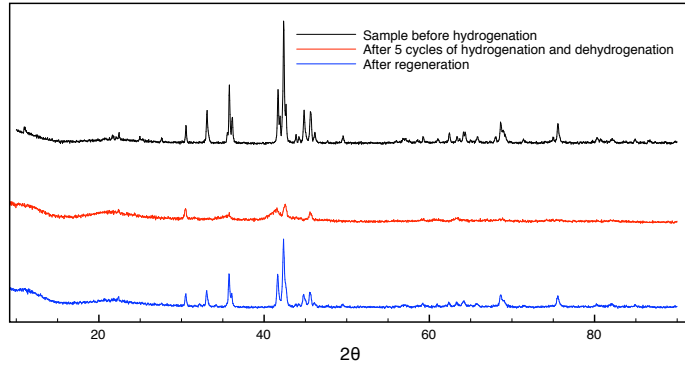
Figure 4.13: *Figure showing the XRD plot for the 30% excess Mg sample melt spun at 1000 RPM. The conditions are before any hydrogenation, after cycling several times, and after regeneration of the sample.*

the other investigation methods, mainly XRD. The results are shown in Figures 4.15-4.17. To be noted is that all the images are taken with the backscatter detector showing phase contrast due to atomic number (Z contrast). This makes it fairly easy to distinguish phases with large difference in Z-value such as, in this work, La_2MgNi_9 and $LaNi_5$ (31.5 vs 32.8). If phases have a very small variation in Z-value, they are hard to distinguish. This is the case for the La_2MgNi_9 and the La_3MgNi_{14} (31.5 vs 31.9). The fact that these samples are synthesized by a non-equilibrium method complicates the picture even more. This may make it possible for more intermediate phases, for example AB_3 and A_2B_7 phases with varying Mg content, making the Z-value vary over the areas of the ternary alloys with La, Mg and Ni.

In Figure 4.14, the image for the as cast sample is shown. The image shows a multiphase structure with at least three phases. These are identified through EDX to be $LaMgNi_4$ (A), La_2MgNi_9 (B) and $LaNi_5$ (C).

In Figure 4.15, the images show the 0% excess Mg samples spun at a) 400 RPM and b) 1000 RPM. Both of the samples are here seen to be mainly built up of La_2MgNi_9 (B) and $LaNi_5$ (C) phases. There is also a small fraction of $LaMgNi_4$ phase, and this is mainly found on the interface between the two other phases. For the 1000 RPM sample, in Figure 4.15(b), the bright $LaNi_5$ (C) phase seems to have grown as a dendritic phase with La-Mg-Ni type phases forming between the dendrites. This is not evident for the 400 RPM sample in Figure 4.15(a).

In Figure 4.16, the images for the 15% excess Mg samples spun at a) 400 RPM and b) 1000 RPM are shown. The samples are mostly built up of the La_2MgNi_9
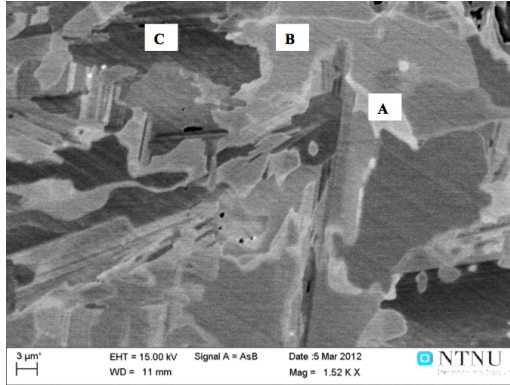
Figure 4.14: *Figure showing the 0% excess Mg sample as as-cast (A-LaMgNi$_4$, B-La$_2$MgNi$_9$, C-LaNi$_5$).*
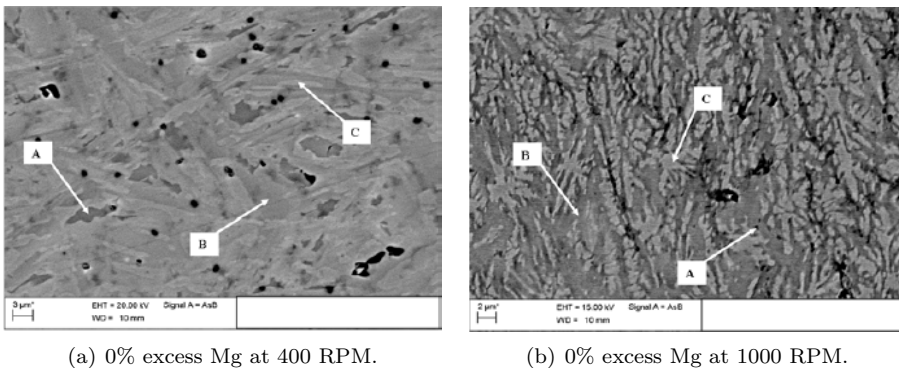
(a) 0% excess Mg at 400 RPM.

(b) 0% excess Mg at 1000 RPM.

Figure 4.15: *SEM pictures of the samples with 0% excess Mg (A-LaMgNi$_4$, B-La$_2$MgNi$_9$, C-LaNi$_5$).*

and LaNi$_5$ phases and seem to be practically a two-phase material. However, some small fractions of LaMgNi$_4$ phase can be found on the interfaces between the two main phases. They are not to be confused with the large black areas in the 400 RPM image (Figure 4.16(a)), where the black areas are voids in the material. A special feature in the 400 RPM image (Figure 4.16(a)) is that the LaNi$_5$ phase seems to have small areas with the La$_2$MgNi$_9$ phase. Some trouble is expected in identifying such small phase areas through the EDX method since the EDX measurement usually has a immersion volume of about $1\mu m$ in radius. The 1000 RPM image (Figure 4.16(b)) is very similar to the 1000 RPM image

for the 0% excess Mg sample (Figure 4.15(b)), and again the dendritic shape of the LaNi$_5$ (C) phase is visible in contrast to the more plate-like LaNi$_5$ (C) phase for this 400 RPM phase shown in Figure 4.16(a).
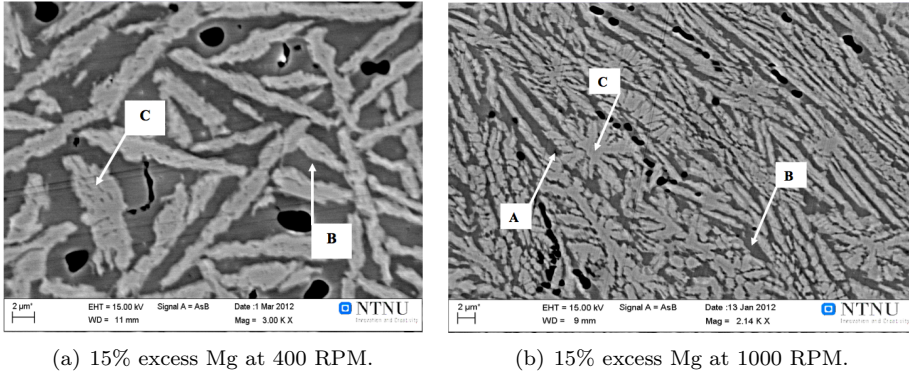

(a) 15% excess Mg at 400 RPM.
(b) 15% excess Mg at 1000 RPM.

Figure 4.16: *SEM pictures of the samples with 15% excess Mg (A-LaMgNi$_4$, B-La$_2$MgNi$_9$, C-LaNi$_5$).*

In Figure 4.17, the images for the 30% excess Mg samples spun at a) 400 RPM and b) 1000 RPM is shown. Here, the images are quite different from the 0% excess and 15% excess Mg samples. The 400 RPM image (Figure 4.17(a)) is quite homogeneous compared to the other two samples spun at 400 RPM, especially the one for the 15% excess Mg alloys (Figure 4.16(a)). Here, there is a much smaller fraction of the bright LaNi$_5$ (C) phase and instead, large phase areas with the La$_2$MgNi$_9$ (B) phase. The image for the 1000 RPM sample (Figure 4.17(b)) shows a more heterogeneous sample than the 400 RPM image, but is still more homogeneous than the samples with 0% excess and 15% excess Mg. It has some more LaNi$_5$ (C) phase areas but still large and dominating areas with the La$_2$MgNi$_9$ (B) phase. This phase also has a significant fraction of a darker phase, which is expected to be the LaMgNi$_4$ (A) phase.
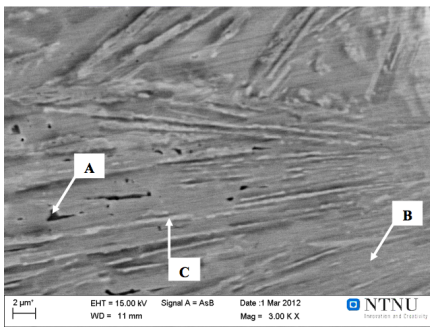
(a) 30% excess Mg at 400 RPM.
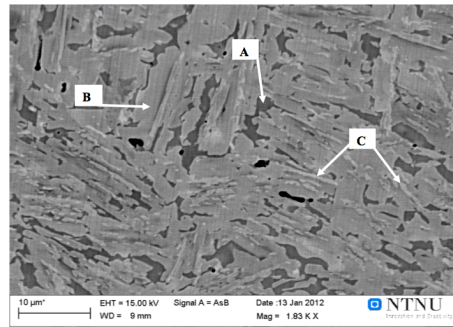
(b) 30% excess Mg at 1000 RPM.

Figure 4.17: *SEM pictures of the samples with 30% excess Mg (A-LaMgNi$_4$, B-La$_2$MgNi$_9$, C-LaNi$_5$).*

Chapter 5

Discussion

5.1 The effect of melt spinning on abundances of the phases

As the $LaNi_5$ phase is a congruent melting phase and the La_2MgNi_9 and La_3MgNi_{14} phases are peritectic phases, the relative abundance of these three phases are key to understanding how the solidification has worked. During solidification, the $LaNi_5$ phase is the phase solidifying at the highest temperature and is therefore expected to be the first phase to be formed. The samples that are solidified through melt spinning have very little time to perform the peritectic transformation from the $LaNi_5$ phase to the La_2MgNi_9 and La_3MgNi_{14} (or other) phases. This is because this transformation has to happen at the solid-liquid interface in the sample. In total one would therefore expect the melt spinning to lead to more and more non-equilibrium phases and consequently to a larger fraction of $LaNi_5$. Contrary to this, another effect is also central during the solidification. This is that the large undercooling during melt spinning also allows a much higher rate of nucleation making the total solid-liquid interface larger in the melt spun samples compared to samples cooled more slowly. The effect of melt spinning is therefore not straightforward to determine. Due to the many possible effects it may be possible to find an optimized process for obtaining as close as possible to a single-phase alloy of La_2MgNi_9-type through melt spinning. The $LaMgNi_4$ phase is expected to be the last phase to solidify. This will happen from pockets of melt with larger fractions of La and Mg. These pockets are expected to arise because of the presence of earlier solidified $LaNi_5$ phase as this phase is richer in Ni than the total composition.

5.1.1 Stoichiometric La$_2$MgNi$_9$ sample with no excess of Mg

For the 0% excess Mg alloy, there are five different samples, the as-cast sample, two annealed samples (at 900°C and 950°C) and three melt spun samples (400 RPM, 1000 RPM and 2000 RPM). All the samples are made from the same starting point, which is the as-cast alloy, this makes it suitable to study the effects of the different treatments. The sample annealed at 950°C is considered as the equilibrium phase for the total composition of this 0% excess Mg. This sample is a two-phase alloy consisting of about 60% La$_2$MgNi$_9$ and 40% La$_3$MgNi$_{14}$. Since the resulting phase abundances from the annealed sample is not a single-phase sample, it is concluded that this phase must have lost some Mg during the processing and has therefore too little Mg to reach a single-phase La$_2$MgNi$_9$ compound. This was possibly lost during the production of the alloy through induction melting. Due to the lack of Mg it was decided to add excess Mg in new samples and this resulted in the samples with 15% and 30% excess Mg. The annealed sample at 950°C was in any case used as a reference to see the effect of melt spinning as compared to the as-cast or annealed samples. The ideal sample produced through melt spinning is the sample with least LaNi$_5$ phase and most possible fraction of the two phases La$_2$MgNi$_9$ and La$_3$MgNi$_{14}$ phase.

As seen in Table 4.1, compared to the annealed sample, the as-cast sample consists of a rather large fraction of LaNi$_5$ and necessarily less La$_2$MgNi$_9$ and La$_3$MgNi$_{14}$ phase. A small fraction of LaMgNi$_4$ makes the total phase composition equal to the annealed sample. These phase abundances suggest that the sample is away from the equilibrium. This is expected, as the production of this alloy did not involve a very slow cooling. The total composition based on these data is La$_{1.96}$Mg$_{0.81}$Ni$_9$. This is similar to the values for the annealed sample at 950°C, La$_{1.97}$Mg$_{0.85}$Ni$_9$. The SEM image for this alloy in Figure 4.14 clearly shows a multiphase structure as suggested by the XRD data. It shows large fractions of LaNi$_5$ and La$_2$MgNi$_9$ phases, where the La$_2$MgNi$_9$ phase abundance may also consist of the La$_3$MgNi$_{14}$ phase. This largely confirms the XRD data.

For the sample melt-spun at low speed (400 RPM), the phase abundances have changed somewhat from the as-cast sample. There is slightly less La$_2$MgNi$_9$ (42.8 vs 50%) and more La$_3$MgNi$_{14}$, less LaNi$_5$ and very little LaMgNi$_4$. If one calculates the relative fractions for the La$_2$MgNi$_9$ and La$_3$MgNi$_{14}$ phase, the ratio is 1.36 (42.8/31.5). For the annealed sample, the comparable value is the same, 1.36. This may suggest that the solidification conditions are actually suitable for obtaining the equilibrium phase compositions had it not been for too fast nucleation and growth of the LaNi$_5$ phase. The SEM image for this phase, in Figure 4.15(a), is relatively poor in contrast. It is possible to separate

three phases in the image as indicated by the letters. The sample seems to be dominated by the La-Mg-Ni phases and the $LaNi_5$ phase as is also indicated by the XRD results.

For the high speed melt spinning, 1000 RPM, one obtains a very large fraction of La_2MgNi_9 phase, and this value is very close to the value for the annealed sample. However, instead of a large quantity of La_3MgNi_{14} phase, a lot of $LaNi_5$ is found. This sample has therefore pushed the total composition slightly more to Ni rich total composition as compared to the value for the as-cast and annealed sample. This indicates that there either should be more of a La-Mg rich phase, such as $LaMgNi_4$, or that part of the sample could have been amorphisized. The SEM image for this sample in Figure 4.15(b) is different from the images of the 400 RPM sample. Here, it is clear that the solidification has occurred at a very fast rate. The phase that forms first, the $LaNi_5$ phase, has solidified in a dendritic manner. The occurrence of a dendritic phase may be coupled with the fact that for this sample, the XRD data shows large quantities of $LaNi_5$ phase. Due to rapid growth of $LaNi_5$ phase, the La-Mg-Ni phases don't have time to form in the solid-liquid interface between $LaNi_5$ phase and the liquid phase resulting in larger fractions of $LaNi_5$ phase. The other phases present are dominated by the La-Mg-Ni phases as suggested by the XRD data.

The very high spinning speed (2000 RPM) was shown through TEM in earlier work [34] to give some degree of amorphization. This led to the conclusion that the phase abundances obtained through Rietveld analysis of the XRD data are not completely accurate and representative for the total sample. No more work was therefore done using the 2000 RPM spin speed.

In total, the results suggest that the spin speed 400 RPM was the ideal spin speed of the ones used. This sample had the phase fractions closest to the value for the annealed sample and was better than the as-cast sample in regards to the amount of $LaNi_5$. The 400 RPM spin speed also avoided the formation of dendritic $LaNi_5$ phase, instead getting a result closer to the result found for the annealed sample.

5.1.2   15% excess Mg samples

For these samples (shown in Table 4.2), the sample melt spun at 400 RPM shows a very promising result. This sample has a very high fraction of La_2MgNi_9 (68.7%), indicating that the addition of extra Mg is a step in the right direction. This sample has also very little $LaNi_5$ phase, but a relatively large amount of $LaMgNi_4$ phase (17.0%). This may indicate that the solidification is close to ideal for rapidly solidified samples, and actually suggest that there is not enough $LaNi_5$

available to get more of the La_2MgNi_9 phase. This will result in a small fraction of $LaNi_5$ and a larger fraction of rest-melt, resulting in the $LaMgNi_4$ phase. The total composition is quite close to the desired composition, $La_{2.02}Mg_{1.09}Ni_9$, so the addition seems quite successful. The SEM image in Figure 4.16(a) shows a sample that looks predominantly like a two-phase compound. It consists of large plate-like fractions of $LaNi_5$ phase in a La-Mg-Ni matrix. This phase has small dark spots in the large $LaNi_5$ areas suggesting the presence of a La-Mg-Ni phase inside the $LaNi_5$ phase. A possible explanation for this is that a relatively rapid solidification leads to small pockets of Mg-rich melt inside the $LaNi_5$ phase. These pockets have not had the time to diffuse into the rest of the melt, leading to small areas of La-Mg-Ni phase inside the $LaNi_5$ phase. Although the image shows a two-phase compound where the fraction of $LaNi_5$ seems to be at least 40%, the XRD results show that the fraction is in fact much smaller. This may be because the enclosed La-Mg-Ni phase is actually a large part of the $LaNi_5$ phase. However, the small fraction of 8.2 wt% as suggested by the XRD data may not be completely compatible with what is visible in the SEM figure.

For the 1000 RPM sample, the phase abundances are quite different from the 400 RPM sample. Here, the La_2MgNi_9 fraction is decreased to allow place for large fractions of $LaNi_5$ (33.5%) and La_3MgNi_{14} phase (20.3%). The total composition suggests that there is too little Mg again. This may be due to some amorphization during the rapid solidification making the phase abundances wrong. Amorphization is, however, not visible in the XRD spectra. The total composition is as poor as $La_{1.92}Mg_{0.58}Ni_9$, and such a large loss of Mg is not well explained from the loss of Mg during melting at least not compared to the 400 RPM sample of the same composition. The image for this sample, in Figure 4.16(b), shows a two-phase compound dominated by a bright $LaNi_5$ phase. According to the XRD data, the $LaNi_5$ phase has the highest abundance among all the samples for this sample, and this is largely confirmed by the SEM image. The fact that the total composition looks to be substantially different from the original stoichiometry may be because of the formation of the dendritic shaped $LaNi_5$. This $LaNi_5$ suggests very fast growth of the solid phase during solidification and may also give rise to a lot of non-equilibrium situations like the pockets of Mg-rich melt in the 400 RPM sample for this composition. The loss can therefore be compensated for if the La-Mg-Ni phases are slightly richer in Mg than the XRD data suggests. Some Mg can even be locked into the $LaNi_5$ phase as even smaller pockets than the ones visible for the 400 RPM sample.

5.1.3 30% excess Mg samples

For these samples, the data are plotted in Table 4.3. As for the 15% excess samples, the 400 RPM spin rate consists a large fraction of the La_2MgNi_9 phase. In this case however, the most abundant secondary phase is the La_3MgNi_{14} phase suggesting that the overall composition is close to La_2MgNi_9, and it is calculated to be $La_{2.01}Mg_{0.97}Ni_9$. This sample is therefore the sample with the total composition closest to La_2MgNi_9. This value is even better than the values obtained for the sample with 15% excess Mg. The sample has a very small total fraction of $LaNi_5$ and $LaMgNi_4$ (14.8%) suggesting that the sample may prove itself to be a very good choice as an electrode alloy. The SEM image for this sample, in Figure 4.17(a), shows that the sample is quite different from the samples with lower Mg content. This sample has small plate-like $LaNi_5$ areas in a largely La-Mg-Ni phase matrix. This distribution is confirmed by the large fractions of the La_2MgNi_9 and the La_3MgNi_{14} phases suggested from the XRD data. These plate-like $LaNi_5$ areas look directional in the sample. The sample has some areas of the Mg-rich $LaMgNi_4$ phase, and these are located in the La-Mg-Ni phase and only rarely borders the $LaNi_5$ suggesting that this is the last Mg-rich melt that solidifies.

For the 1000 RPM sample, there is very little La_3MgNi_{14} phase in the sample, but a large amount of the La_2MgNi_9 phase (79.2%). This sample is the melt-spun alloy with the largest abundance of the La_2MgNi_9 phase. Here, the additional phases are dominated by a relatively large fraction of $LaNi_5$ phase. The total composition is $La_{1.86}Mg_{0.84}Ni_9$, which is much better than the composition for the 15% excess Mg sample melt spun at 1000 RPM. It still differs slightly from the composition for 400 RPM with 30% excess Mg, suggesting perhaps some degree of amorphization. The SEM image for this sample, Figure 4.17(b), shows a sample largely dominated by the La-Mg-Ni phase. Here, there are plate-like areas of $LaNi_5$ phase inside the La-Mg-Ni phase, as was also visible in the 400 RPM sample for the same composition. There are, however, quite large areas of the Mg-richer $LaMgNi_4$ phase suggesting that the $LaNi_5$ phase abundance also is larger than for the 400 RPM sample. This $LaMgNi_4$ is again situated only bordering to the La-Mg-Ni phase suggesting that this is the phase that solidifies last.

5.1.4 Concluding remarks about phase abundances

In the XRD data and the SEM data, it can be seen that the phase abundances and type of solidification is both dependent on the composition of the sample and the spinning speed. A spinning speed of 400 RPM appears to yield a better

result for all the compositions. It is therefore concluded that the higher spinning speed of 1000 RPM will normally give larger fractions of LaNi$_5$ phase reducing the fraction of the desired La$_2$MgNi$_9$ and La$_3$MgNi$_{14}$ phases. This is further supported by the appearance of dendritic shaped LaNi$_5$ phase for the 0% and 15% excess Mg compositions spun at 1000 RPM. The dendritic phase suggests a very high solidification velocity giving too high a content of the phase first solidifying, the LaNi$_5$ phase. For future work, it may be noted that the presence of dendritic shaped LaNi$_5$ phases in such a compositions is considered detrimental to the presence of La$_2$MgNi$_9$ and La$_3$MgNi$_{14}$ phases.

For the total compositions it is concluded that the addition of Mg has been very successful for the samples used. The fraction of LaNi$_5$ decreases due to the increase in Mg content as expected. The XRD results suggest that there is not much difference in the 400 RPM samples for the 15% and 30% excess Mg compositions, but the SEM image suggests that 400 RPM sample is superior. This is important if the pockets of La-Mg-Ni phase in the 15% excess Mg sample account for a large fraction of La-Mg-Ni phase. These may be locked in in a hydrogenation experiment like electrochemical testing, where the LaNi$_5$ phase may not be hydrogenated, and lead to a loss of capacity even though the phase is actually present in the material. Therefore, the sample with 30% excess Mg and 400 RPM spin speed is considered the superior sample. It may be possible to investigate samples using even more Mg or variations around 30% excess Mg. It will also be interesting to check the samples with even lower spin speed, although this was hard to accomplish with the setup at NTNU.

5.2   Thermodynamic properties of the alloys

The commercial AB$_5$ alloy today used in batteries is a variant of the LaNi$_5$ phase with several alloying elements to give the necessary properties for a battery. One important aspect for this phase is that the pure phase normally has a plateau pressure during absorption of more than or equal to 3 bar at room temperature and therefore considerably higher than 1 bar, as is necessary for batteries [37]. The AB$_5$ type batteries are therefore alloyed to achieve a useful plateau pressure and this is not the case for the LaNi$_5$ phase present in the samples presented here. For the La$_2$MgNi$_9$ and La$_3$MgNi$_{14}$ phases, however, this alloying is not necessary. These phases have a transformation pressure between 0.1 and 0.5 bar at room temperature and are therefore theoretically very useful as battery alloys as pure phases. The difference in transformation temperature between the phases can be verified both by checking the alloys during in-situ XRD (Section 4.1.6) and through measuring PCT of the alloys (Section 4.3). This transformation

temperature is directly related to the plateau pressure and the enthalpy of the phases as shown in Equation 2.3.

As can be seen clearly for the in-situ data, especially for the 0% excess Mg 1000 RPM and 0% excess 2000 RPM samples, there is considerable difference in the transformation temperature between the $LaNi_5$ phase and the La_2MgNi_9 and La_3MgNi_{14} phases. This is especially visible in the figures for absorption (Figures 4.6 & 4.8). Here, the transformation temperature difference can be as much as much as 40°C. This difference in transformation temperature could have been visible in PCT as a second plateau due to the $LaNi_5$ phase. This is not visible in the PCTs obtained for the samples and can be due to other factors such as the $LaNi_5$ phase being altered due to the rapid solidification, as suggested by the cell parameters, or local conditions in the material during the PCT run may alter the plateau pressure. Due to the instability of the samples due to cycling, the thermodynamic values were hard to calculate from the data obtained. However, the curves obtained for 25°C can be compared to the values obtained in the work by Denys et al [2] for the La_2MgNi_9 sample. In Figure 5.1 this is done for the sample with 30% excess Mg melt spun at 400 RPM. Here, the desorption curves at 25°C are plotted alongside the curves obtained in the work by Denys et al, where the temperature was 20°C. As the curves obtained in this work are slightly higher in pressure than the curve found by Denys et al as expected by the increase in temperature, the data are concluded to be similar. It is therefore safe to assume that the thermodynamic values obtained in the article can be used to estimate the values for the alloys in this work. These are given as:

$$\Delta H_{abs} = -35.0 \pm 0.8 \frac{kJ}{mol_{H_2}} \tag{5.1}$$

$$\Delta S_{abs} = -99.6 \pm 2.5 \frac{J}{Kmol_{H_2}} \tag{5.2}$$

$$\Delta H_{des} = 35.9 \pm 0.3 \frac{kJ}{mol_{H_2}} \tag{5.3}$$

$$\Delta H_{abs} = 96.7 \pm 0.9 \frac{J}{Kmol_{H_2}} \tag{5.4}$$

Through the transformation temperature difference of 35-45°C, the difference in transformation enthalpy for the phases present can be calculated from Equation 2.3. This yields that such a difference gives a difference in transformation enthalpy, considering constant entropy of 130 J/Kmol, of 3.2-4.4 kJ/mol between the La_2MgNi_9 and $LaNi_5$ phase. This is a significant difference in the enthalpy and is more than enough to make only one of the phases useful in an electrode,
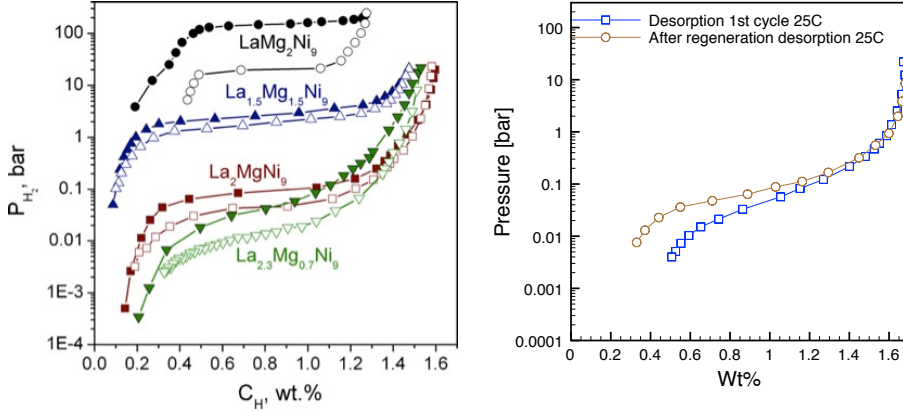
(a) Figure from Denys et al [2], curve recorded (b) PCT curves for the 30% excess Mg sample
at 20°C.   melt spun at 400 RPM (desorption).

Figure 5.1: *Comparison of the PCT curve found in this work with the curves found in the work by Denys et al [2].*

making it very important to try to avoid the presence of the $LaNi_5$ phase.

5.3 Electrochemical capacities

As shown in Table 4.7, the capacities of all the samples are between 220 and 300 mAh/g. This value is relatively low compared to the capacities reported in literature of up to 400 mAh/g. The melt spinning in general may cause the capacity to drop somewhat, but the fact that some of the samples synthesized in this work has a very high fraction of La_2MgNi_9 it is hard to accept that the capacity should drop that much. It is therefore believed that the experimental procedure used here is somewhat different than what is reported in literature. As the charge and discharge current is very low in this work, one has to look at other factors.

The different phases have different properties concerning electrochemistry. The most important factor is that the hydride must not be too stable or too unstable at room temperature. The $LaNi_5$ phase does not work in this respect, this phase normally have a plateau pressure at room temperature above 1 bar [37]. This makes it impossible for the phase to be hydrogenated at room temperature in the electrochemical setup used here. However, this plateau pressure may be

altered because the $LaNi_5$ phase seems to have a slightly distorted structure with elongation in the c direction and compression in the a directions. This distortion is not compatible with the data available on non-stoichiometric $LaNi_5$ phase as shown in Section 4.1.5, but it may be due to the production method, creating slightly distorted structures. The $LaMgNi_4$ is also a problematic phase, this phase undergoes a hydrogen-induced amorphization leading to a very stable hydride and thereby making it hard to dehydrogenate the phase. This phase is therefore practically irreversible at room temperature.

The La_2MgNi_9 and La_3MgNi_{14} phases have similar and useful plateau pressures below 1 bar at room temperature. These phases does also have a high gravimetric storage capacity due to the Mg in the phases, making the phase lighter than the $LaNi_5$ phase. These phases may however have some variation in the stoichiometry, and a relatively small variation in the Mg content in the phase may give a tenfold change in plateau pressure as shown by Denys et al [2]. What is therefore expected is that the fraction of the two phases La_2MgNi_9 and La_3MgNi_{14} combined should determine the maximum reversible electrochemical capacity.

Below in Table 5.1, the total fraction of the La_2MgNi_9 and La_3MgNi_{14} phases are shown compared with the maximum capacity.

Table 5.1: *The maximum electrochemical capacity measured for the samples compared with the total abundance of La_2MgNi_9 and La_3MgNi_{14} phases.*

Alloy	Spin rate [RPM]	Max capacity $[\frac{mAh}{g}]$	Abundance of useful phases [wt%]	La_2MgNi_9 [wt%]
$La_2Mg_1Ni_9$+0%	1000	259	75.1	58.7
	2000	223	88.7	57.0
$La_2Mg_1Ni_9$+15%	400	290	74.7	68.7
	1000	271	66.6	46.3
	400	297	85.2	71.2
$La_2Mg_1Ni_9$+30%	1000	251	84.8	79.2

The table shows clearly that the expectation given in the above paragraph is not correct in our experiments. The maximum capacity is therefore also determined by some other factor or factors. There is another trend visible in the data, it seems that a reduction in spinning speed always lead to a higher capacity. Even between samples with the same spinning speed, there seems to be no correlation between the fraction of La_2MgNi_9 and La_3MgNi_{14} phases and the capacity. There was not enough sample available to give good statistics for the different samples. This

may pose a problem as the material chosen from the sample may be especially poor or good.

The result that the capacity seems to be dependent on the spinning speed may be due to the fact that a higher melt spinning speed will give more interfaces. The increase in interfaces should lead to better sorption kinetics, but for low rates of hydrogenation and dehydrogenation this is not an important factor. With such a situation, the increase in interfaces could instead lead to a larger fraction of the material being oxidized or in some other way degraded during electrochemical charge-discharge cycling leading to a total decrease in capacity compared to the sample prepared at lower spinning speed.

5.4   Stability of the hydrogenated phases

As both the cycling data for the 30% excess Mg sample with 400 RPM spin rate (Figure 4.10) and the PCT data for all of the samples (Figure 4.11) show, the samples show a very poor cyclic stability. After a few cycles with PCT measurement the phase abundances change considerably for all the samples (Figure 4.4). The results demonstrate that the samples show a large degree of amorphization due to the hydrogenation and this is true for both the La_2MgNi_9 and the La_3MgNi_{14} phases. For the $LaNi_5$ phase, the diffraction peaks are clearly still present and the intensities of the peaks are highly dependent on the fraction of $LaNi_5$ phase in the original sample as expected. It is therefore concluded that the La_2MgNi_9 phase goes into some partly or fully amorphous phase. Such amorphous phases have been known to be very stable and consequently very irreversible. However, the PCT data show that although one may expect a capacity loss of 70-80% due to this amorphization, the loss is about 30-40% after 4-5 cycles. This suggests that although the phase goes through a change in structure, some of the capacity is still reversible. This behavior is similar for all the rapidly solidified samples and the change is independent on rapid solidification conditions, it is even visible in the annealed sample as shown in Figure 4.11. This amorphization is therefore not a result of the rapid solidification and is rather a property of the phases in themselves. The reason for the amorphization may be due to the large volume expansion during hydrogenation of the alloy. This volume expansion reaches about 25.5 vol% in the X-ray refinements reported in Table 4.5. If this is the case, such a volume expansion can be reduced by suitable substitution on either A- or B-side of composition.

To reverse this amorphization, a regeneration procedure was tried. The regeneration process was to heat the sample up to 400°C in high vacuum. Most of the desorption from the sample then was finished at around 200-250°C as shown

54

in Figure 4.12. In this figure, the continued desorption starts at once the sample is heated from room temperature and is high until the sample seems to be completely dehydrogenated at 250°C. This indicates that the desorption process occurring during this regeneration is a continuation of the desorption process occurring in vacuum at room temperature. That the reaction is a continuation indicates that the phases desorbing are the phases that have disappeared in the XRD plot after hydrogenation and dehydrogenation.

The regeneration process resulted in that the capacity was restored to the original capacity as shown in Figure 4.12(a) for the 30% excess Mg sample spun at 400 RPM. For the 30% excess Mg sample spun at 1000 RPM, the regeneration gave the XRD results shown in Figure 4.13. Here, one can clearly see that most of the peaks disappear after hydrogenation and dehydrogenation, but after the regeneration process, most of the peaks have reappeared, although not at their original intensities. The peak intensities may be smaller than for the original alloy due to the volume expansion occurring during the hydrogenation process leading to microstrain and change in crystallite size. The integral peak intensities, however, may be the same, but this was not investigated in this work.

Although the original capacity was regained after the regeneration process, cycling led to the same amorphization again so the regeneration did not lead to a reversible and stable sample. The phases influenced by this process were the La_2MgNi_9 and La_3MgNi_{14} phases, and due to this problem, these phases should somehow be stabilized and the plateau pressure should be somewhat increased to ensure complete desorption at room temperature. For example a small amount of Ce and Co can be used as A and B element substitution, respectively. These elements are chosen as Ce is known for reducing the unit cell volume and thereby increase the plateau pressure, while the Co is a well known element used to achieve cyclic stability.

During electrochemical testing, the capacity loss is very much smaller than for the gaseous PCT tests. This may be explained by that the samples are kept at a low temperature during the whole run. It can also be explained by that the samples are kept in a better environment meaning the KOH electrolyte. This may prevent the samples from forming the amorphous phase. Another aspect may be that the slow rate of hydrogenation the samples are exposed to during electrochemical testing is slow enough so that the samples do not form amorphous phase, rather a more reversible La-Mg-Ni-H phase, possibly a La_2MgNi_9 phase.

Chapter 6

Conclusions

Ternary La-Mg-Ni hydrogen storage alloy with a composition La_2MgNi_9 belongs to a new class of materials for the negative electrodes in Ni-Metal Hydride (Ni-MH) batteries with electrochemical discharge capacity reaching 400 mAh/g. This value is 25% superior to the commercial AB_5-type electrodes.

Differences in melting temperature of La, Ni and Mg and a complexity in the phase equilibria in the La-Mg-Ni system cause difficulties in synthesis of a battery electrode with controlled Mg content and a desired phase-structural composition. The goal of this work was to develop efficient synthesis techniques of preparation of a single-phase alloy with the La_2MgNi_9 composition by employing Rapid Solidification technique. Both the initial alloys and their corresponding hydrides were characterized by synchrotron X-ray diffraction (including *in situ* studies in hydrogen gas, performed at Swiss-Norwegian Beam Lines at ESRF, Grenoble), Scanning Electron Microscopy with electron probe microanalysis, Pressure-Composition-Temperature isotherms, hydrogen absorption-desorption cycling and measurements of the electrochemical charge-discharge performances.

This gave the following conclusions:

1) Four phase constituents have been found in the alloys, (I) La_2MgNi_9, (II) La_3MgNi_{14}, (III) $LaNi_5$ and (IV) $LaNi_5$. Two of these, I and II, undergo reversible hydrogenation-dehydrogenation during electrochemical experiments. The other two, III and IV, do not contribute to the electrochemical capacities. Thus, the formation of III and IV should be avoided.

2) The melt spinning process led to a loss of Mg during as compared to the

initial mixtures, and the addition of excess Mg was conducted and proved to be a successful way to compensate for this loss in order to arrive at the desired compositions. The best yield of La_2MgNi_9 phase was achieved when 30% weight excess of Mg as compared to the stoichiometric ratio was added.

3) Both 400 and 1000 RPM wheel spin speed of the sample with 30% excess Mg provide the samples with the best homogeneities, highest content of La_2MgNi_9 and the smallest concentrations of $LaNi_5$ and $LaMgNi_4$ phases. The highest content of La_2MgNi_9 synthesized was close to 80 wt%.

4) Through the studies of the PCT diagrams it was found a good correspondence between the data of the measurements and earlier published results by R.V. Denys and V.A. Yartys [2]. From these measurements the reversible hydrogen storage capacity was found to be between 1.4 and 1.5 wt%.

5) The cycling of the samples in gaseous hydrogen showed a decay in the reversible capacities caused by loss of crystallinity and formation of the (partially) amorphous products of the La_2MgNi_9 phase. This was considered to be an intrinsic property of the studied alloy and not a result of the conditions used during the synthesizing of the samples. The loss of crystallinity is most likely related to the large hydrogenation-induced volume expansion.

6) However, the regeneration of the original crystalline La_2MgNi_9 phase was possible and was achieved by vacuum heating up to 450°C causing hydrogen desorption and crystallization of the initial intermetallic alloy. This led to the complete recovery of the original hydrogen storage behaviors and H capacities.

7) The electrochemical testing showed strong dependence of the charge-discharge behaviors on the quenching conditions used during the synthesis. A slow spinning speed of 400 RPM always yielded a better electrochemical performance than the 1000 RPM spinning speed, and the best result was reached for the sample with 30% excess Mg spun at 400 RPM.

8) The electrochemical cycling of the samples showed better stability with respect to delay of the charge-discharge performance as compared with gaseous hydrogen. The best capacity was reached for the sample containing 30% excess Mg spun at 400 RPM.

9) Further studies will be required to uncover the reasons for the differences in the behaviors between the as-cast and annealed samples on one side and the rapidly solidified material on the other side. One possibility for the observed variations of properties could be the presence of a partially amorphous constituents in the RS alloys that could affect the hydrogen charge-discharge properties. A short term heating to 300-450°C should be tried in order to achieve crystallization of this amorphous component.

Bibliography

[1] S. De Negri, M. Giovannini, and A. Saccone. Phase relationships of the La-Ni-Mg system at 500C from 66.7 to 100at% Ni. *Journal of Alloys and Compounds*, 439(1-2):109 – 113, 2007.

[2] R.V. Denys and V.A. Yartys. Effect of magnesium on the crystal structure and thermodynamics of the La3-xMgxNi9 hydrides. *Journal of Alloys and Compounds*, 509, Supplement 2(0):S540 – S548, 2011. Proceedings of the 12th International Symposium on Metal-Hydrogen Systems, Fundamentals and Applications (MH2010).

[3] L. Lemort. *Elaboration et caractérisation d'alliages hydrurables de type ABx Elaboration et charactérisation d'alliages hydrurables de type ABx (A=Pr, Nd, La, Mg; B=Ni; x=3,3.5,3.8,5) en vue de leur utilisation comme matière active pour électrode négative d'accumulateurs NiMH.* PhD thesis, L'Universite de Parie-Est Creteil, 2010.

[4] K.H.J. Buschow, P.C.P. Bouten, and A.R. Miedema. Hydrides formed from intermetallic compounds of two transition metals: a special class of ternary alloys. *Reports on Progress in Physics*, 45(9), 1982.

[5] H. Uchida, M. Tada, and Y.C. Huang. The influence of cerium, praseodymium, neodymium and samarium on hydrogen absorption in LaNi5 alloys. *Journal of the Less Common Metals*, 88(1):81 – 87, 1982. International Symposium on the Properties and Applications of Metal Hydrides.

[6] T. Sakai, H. Yoshinaga, H. Miyamura, N. Kuriyama, and H. Ishikawa. Rechargeable hydrogen batteries using rare-earth-based hydrogen storage alloys. *Journal of Alloys and Compounds*, 180(1-2):37 – 54, 1992.

[7] L.O. Valoen. *Metal Hydrides for Rechargeable Batteries.* PhD thesis, Norwegian University of Science and Technology, 2000.

[8] F. Zhang, Y. Luo, A. Deng, Z. Tang, L. Kang, and J. Chen. A study on structure and electrochemical properties of (La, Ce, Pr, Nd)2MgNi9 hydrogen storage electrode alloys. *Electrochimica Acta*, 52(1):24 – 32, 2006.

[9] Y. Li, D. Han, S. Han, X. Zhu, L. Hu, Z. Zhang, and Y. Liu. Effect of rare earth elements on electrochemical properties of La-Mg-Ni-based hydrogen storage alloys. *International Journal of Hydrogen Energy*, 34(3):1399 – 1404, 2009.

[10] F. Feng, M. Geng, and D.O. Northwood. Electrochemical behaviour of intermetallic-based metal hydrides used in Ni/metal hydride (MH) batteries: a review. *International Journal of Hydrogen Energy*, 26(7):725 – 734, 2001.

[11] Y. Liu, H. Pan, M. Gao, Y. Zhu, Y. Lei, and Q. Wang. The electrochemical performance of a La-Mg-Ni-Co-Mn metal hydride electrode alloy in the temperature range of 20 to 30C. *Electrochimica Acta*, 49(4):545 – 555, 2004.

[12] N. Cui, P. He, and J.L. Luo. Magnesium-based hydrogen storage materials modified by mechanical alloying. *Acta Materialia*, 47(14):3737 – 3743, 1999.

[13] D.-M. Kim, K.-J. Jang, and J.-Y. Lee. A review on the development of AB2-type Zr-based Laves phase hydrogen storage alloys for Ni-MH rechargeable batteries in the Korea Advanced Institute of Science and Technology. *Journal of Alloys and Compounds*, 293-295(0):583 – 592, 1999.

[14] H. Okamoto. La-Ni (lanthanum-nickel). *Journal of Phase Equilibria*, 23(3):287–288, 2002.

[15] T. Yamamoto, H. Inui, M. Yamaguchi, K. Sato, S. Fujitani, I. Yonezu, and K. Nishio. Microstructures and hydrogen absorption/desorption properties of LaNi alloys in the composition range of La77.8-83.2 at.% Ni. *Acta Materialia*, 45(12):5213 – 5221, 1997.

[16] J.J. Reilly, G.D. Adzic, J.R. Johnson, T. Vogt, S. Mukerjee, and J. McBreen. The correlation between composition and electrochemical properties of metal hydride electrodes. *Journal of Alloys and Compounds*, 293-295:569 – 582, 1999.

[17] T. Kohno, H. Yoshida, F. Kawashima, T. Inaba, I. Sakai, M. Yamamoto, and M. Kanda. Hydrogen storage properties of new ternary system alloys: La2MgNi9, La5Mg2Ni23, La3MgNi14. *Journal of Alloys and Compounds*, 311(2):L5 – L7, 2000.

[18] B. Liao, Y.Q. Lei, G.L. Lu, L.X. Chen, H.G. Pan, and Q.D. Wang. The electrochemical properties of LaxMg3-xNi9 (x=1.0-2.0) hydrogen storage alloys.

Journal of Alloys and Compounds, 356-357(0):746 – 749, 2003. Proceedings of the Eighth International Symposium on Metal-Hydrogen Systems, Fundamentals and Applications (MH2002).

[19] H. Pan, Y. Liu, M. Gao, Y. Zhu, Y. Lei, and Q. Wang. An investigation on the structural and electrochemical properties of La0.7Mg0.3(Ni0.85Co0.15)x (x=3.15-3.80) hydrogen storage electrode alloys. *Journal of Alloys and Compounds*, 351(1-2):228 – 234, 2003.

[20] F. Zhang, Y. Luo, D. Wang, R. Yan, L. Kang, and J. Chen. Structure and electrochemical properties of La2-xMgxNi7.0 (x=0.3-0.6) hydrogen storage alloys. *Journal of Alloys and Compounds*, 439(1-2):181 – 188, 2007.

[21] J.F. Stampfer, C.E. Holley, and J.F. Suttle. The magnesium-hydrogen system1-3. *Journal of the American Chemical Society*, 82(14):3504–3508, 1960.

[22] R.V. Denys, A.B. Riabov, V.A. Yartys, M. Sato, and R.G. Delaplane. Mg substitution effect on the hydrogenation behaviour, thermodynamic and structural properties of the La2Ni7-H(D)2 system. *Journal of Solid State Chemistry*, 181(4):812 – 821, 2008.

[23] Y. Liu, Y. Cao, L. Huang, M. Gao, and H. Pan. Rare earth-Mg-Ni-based hydrogen storage alloys as negative electrode materials for Ni/MH batteries. *Journal of Alloys and Compounds*, 509(3):675 – 686, 2011.

[24] E. Akiba, H. Hayakawa, and T. Kohno. Crystal structures of novel La-Mg-Ni hydrogen absorbing alloys. *Journal of Alloys and Compounds*, 408-412:280 – 283, 2006. Proceedings of Rare Earths'04 in Nara, Japan, Proceedings of Rare Earths'04.

[25] V.A. Yartys, A.B. Riabov, R.V. Denys, M. Sato, and R.G. Delaplane. Novel intermetallic hydrides. *Journal of Alloys and Compounds*, 408-412(0):273 – 279, 2006. Proceedings of Rare Earths'04 in Nara, Japan.

[26] J. Zhang, B. Villeroy, B. Knosp, P. Bernard, and M. Latroche. Structural and chemical analyses of the new ternary La5MgNi24 phase synthesized by Spark Plasma Sintering and used as negative electrode material for Ni-MH batteries. *International Journal of Hydrogen Energy*, 37(6):5225 – 5233, 2012. Optimization Approaches to Hydrogen Logistics.

[27] J. Chen, H.T. Takeshita, H. Tanaka, N. Kuriyama, T. Sakai, I. Uehara, and M. Haruta. Hydriding properties of LaNi3 and CaNi3 and their substitutes with PuNi3-type structure. *Journal of Alloys and Compounds*, 302(1-2):304 – 313, 2000.

[28] D.W. Oxtoby. Homogeneous nucleation: theory and experiment. *Journal of Physics: Condensed Matter*, 4(38):7627, 1992.

[29] A.L. Greer. Grain refinement in rapidly solidified alloys. *Materials Science and Engineering: A*, 133:16 – 21, 1991. Proceedings of the Seventh International Conference on Rapidly Quenched Materials.

[30] E.J. Lavernia and T.S. Srivatsan. The rapid solidification processing of materials: science, principles, technology, advances, and applications. *Journal of Materials Science*, 45(2):287–325, 2010.

[31] R. Trivedi, S.H. Han, and J.A. Sekhar. Microstructural development in interfiber regions of directionally solidified composites. *Solidification of metal matrix composites; Proceedings of the Conference, Indianapolis, IN; UNITED STATES; 1-5 Oct. 1989*, 1990.

[32] R. Mishima, H. Miyamura, T. Sakai, N. Kuriyama, H. Ishikawa, and I. Uehara. Hydrogen storage alloys rapidly solidified by the melt-spinning method and their characteristics as metal hydride electrodes. *Journal of Alloys and Compounds*, 192(1-2):176 – 178, 1993.

[33] W.H. Bragg and W.L. Bragg. The Reflection of X-rays by Crystals. *Proceedings of the Royal Society of London A*, 88:428–438, 1913.

[34] T. Holm. Crystal structure of RE-Mg-Ni alloys after Rapid Solidification. Master's thesis, NTNU, 2011.

[35] S. Gulbrandsen-Dahl. *Rapid Solidification of AB5 Hydrogen Storage Alloys*. PhD thesis, Norwegian University of Science and Technology, 2002.

[36] P.H.L. Notten, R.E.F. Einerhand, and J.L.C. Daams. On the nature of the electrochemical cycling stability of non-stoichiometric LaNi5-based hydride-forming compounds Part I. crystallography and electrochemistry. *Journal of Alloys and Compounds*, 210:221 – 232, 1994.

[37] J.-M. Joubert, R. Cerny, M. Latroche, E. Leroy, L. Guenee, A. Percheron-Guegan, and K. Yvon. A Structural Study of the Homogeneity Domain of LaNi5. *Journal of Solid State Chemistry*, 166(1):1 – 6, 2002.

Appendix A

Presentation during SYNKNOYT 2012

The work done during the autumn project along with some of the work presented in this report were used in a presentation at the SYNKNOYT conference held by Norges Forskningsrad (NFR) during the 30.-31. January 2012. The webpage of the program is at:

www.forskningsradet.no/synkrotron

Below is the abstract of the presentation:

Rapidly Solidified (La,Mm)-Mg-Ni AB$_3$ and A$_2$B$_7$-type Alloys for the Ni-Metal Hydride batteries studied by Synchrotron X-Ray Diffraction

Although Ni-MH batteries are commercially available and perform satisfactorily for many applications, novel materials with improved energy storage capacities must be identified.

High H/metal ratios, low cost and appealing safety aspects attract interest to use of Mg-based alloys for storage of electrolytic hydrogen. La-Mg-Ni compounds with AB$_3$ and A$_2$B$_7$ types La-Mg-Ni alloys are already utilized in novel Ni-MH batteries. Some of the hydrogen storage, structural and thermodynamic properties of the alloys are characterized [2]. In order to improve the performance of the batteries, three complementary approaches can be applied; (a) Selection of the Rare Earth metal and its content in the alloy; (b) Choice of the content of Mg; (c) Optimisation of the metallurgical route to produce the alloy.

In present work we used lanthanum and Mischmetal (Mm = 58 La, 28.6 Ce, 5.4 Pr and 7.5 wt.% Nd) as rare earth elements and replaced part of the Rare Earths by magnesium to reach compositions RE_2MgNi_9 and RE_3MgNi_{14}. Rapid Solidification was utilized to arrive at a desired phase-structural composition. In total four alloys were used for the melt spinning; La_2MgNi_9 and La_3MgNi_{14}, Mm_2MgNi_9 and Mm_3MgNi_{14}. Mm alloys were produced by arc melting of the Mm-Ni prealloys, which were then ball-milled with magnesium added in excess of 10%. The powders were pressed into pellets and melt-spun in Ar at wheel speed rates of 4.2, 10.9 and 20.9 m/s.

The alloys were characterized by synchrotron XRD at Swiss-Norwegian Beam Lines accommodated at ESRF, Grenoble, France. The ex situ high resolution diffraction data were collected at the beamline BM1B (2θ range 3 - 40 deg.; λ = 0.5023 A). In addition, hydrogen absorption-desorption was studies by in situ SR XRD experiments performed under pressure of hydrogen gas of 10 bar. The data were refined using the General Structure Analysis System software.

The refinements showed formation of multi-phase samples containing: (1) $LaNi_5$, (2) La_2MgNi_9, (3) La_3MgNi_{14}, (4,5) La_4MgNi_{19} (3R and 2H), (6) pure Ni and (7) $LaMgNi_4$. In all studied alloys, the $LaNi_5$- and La_2MgNi_9-intermetallics dominate at the highest melt spin rates (> 80 wt.%), while the La_3MgNi_{14}-phase is present in a large extent at the lowest spin rate (25-30 wt.%) and disappears almost completely at the high spin rates.

In contrast, for the melt spun La_3MgNi_{14} alloy, a large amount of La_4MgNi_{19} intermetallic (around 50 wt.%) was formed at a spin rate of 10.9m/s.

For the RS Mischmetal-based samples, AB_5-type compound was formed in larger quantities than in the La-samples.

The alloys were also characterized by SEM, electrochemical and by PCT studies to establish relations between the phase-structural composition, melt spinning speed and electrochemical performance. The discharge capacity of La_2MgNi_9 reaches 360 mAh/g and with a cycle life of electrode exceeding 300 charge-discharge cycles and shows a great potential of such alloys as materials for the advanced Ni-Metal Hydride batteries.

Appendix B

Article in progress

Below is the abstract of the article in progress based on some of the material presented in this work:

Structural analysis of rapidly-solidified La$_2$MgNi$_9$ hydrogen storage alloys

The phase structure and composition of La$_2$MgNi$_9$ alloy after rapid solidification at spinning rates of 1000 and 400 RPM corresponding to wheel surface speeds of 10.5 and 4.2 ms^{-1} respectively, have been investigated by electron microscopy (SEM, TEM) and X-ray diffraction techniques. This alloy is multi-phase structured containing PuNi$_3$-type La$_2$MgNi$_9$ (space group R$\bar{3}$m) as the main phase with small amounts of LaNi$_5$ and LaMgNi$_4$ as secondary phases. Providing an alloy sample contains the adequate stoichiometric amount of Mg, the tendency to form a single-phase $PuNi_3$-type structure which is desirable for enhanced electrochemical properties, increases at lower cooling rates during solidification as the low thermal gradient and increased diffusion promotes a nearly-homogeneous La$_2$MgNi$_9$ structure with uniformly the same composition as the standard alloy. To compensate for the loss of Mg from the melt due to its low melting point and high vapor pressure relative to other constituent elements, 15% and 30% Mg in excess of the standard stoichiometric quotient were added to separate samples of the alloy respectively.
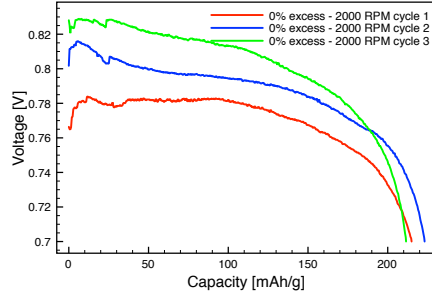
IV

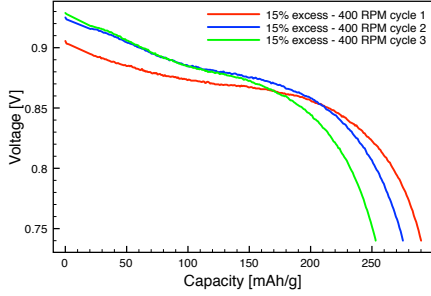# Appendix C

Electrochemical tests

Below in Figure C.1, the electrochemical discharge curves for the first cycles for all the alloys are shown. All samples were tested at the same conditions, with 19mA (29mA/g) discharge current and the same 9M KOH electrolyte and NiOOH counter electrode.
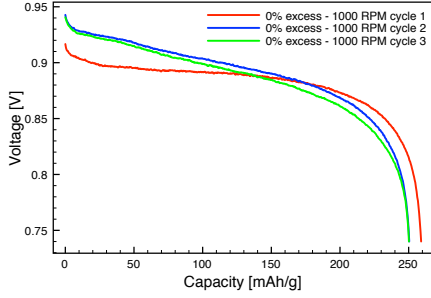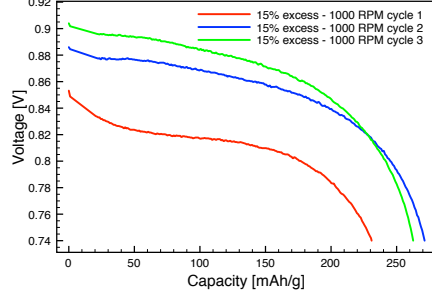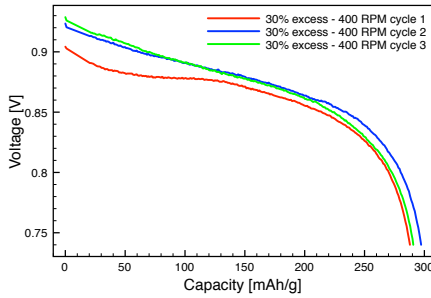
(a) 0% excess Mg at 1000 RPM.
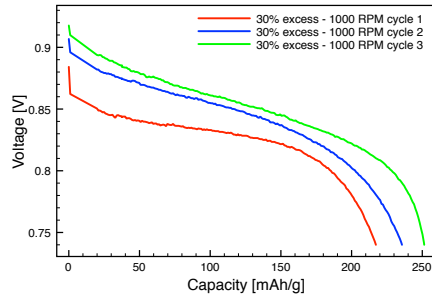
(b) 0% excess Mg at 2000 RPM.

(c) 15% excess Mg at 400 RPM.

(d) 15% excess Mg at 1000 RPM.

(e) 30% excess Mg at 400 RPM.

(f) 30% excess Mg at 1000 RPM.

Figure C.1: *Electrochemical discharge curves for the first cycles for all the samples.*